Analytical and Experimental Characterization of a Linear-Array Thermopile Scanning Radiometer for Geo-Synchronous Earth Radiation Budget Applications

Ira J. Sorensen

Thesis submitted to the Faculty of the

Virginia Polytechnic Institute and State University

in partial fulfillment of the requirements for the degree of

Master of Science

in

Mechanical Engineering

Dr. J.R. Mahan, Chair

Dr. Brian Vick

Dr. Kory J. Priestley

December 4, 1998

Blacksburg, Virginia

Keywords: radiometry, thermopile radiation detectors, Earth radiation budget

Analytical and Experimental Characterization of a Linear-Array Thermopile Scanning Radiometer for Geo-Synchronous Earth Radiation Budget Applications

Ira J. Sorensen

J. Robert Mahan, Chair

Mechanical Engineering

(ABSTRACT)

The Thermal Radiation Group, a laboratory in the department of Mechanical Engineering at Virginia Polytechnic Institute and State University, is currently working towards the development of a new technology for cavity-based radiometers. The radiometer consists of a 256-element linear-array thermopile detector mounted on the wall of a mirrored wedge-shaped cavity. The objective of this research is to provide analytical and experimental characterization of the proposed radiometer. A dynamic end-to-end opto-electrothermal model is developed to simulate the performance of the radiometer. Experimental results for prototype thermopile detectors are included. Also presented is the concept of the discrete Green's function to characterize the optical scattering of radiant energy in the cavity, along with a data-processing algorithm to correct for the scattering. Finally, a parametric study of the sensitivity of the discrete Green's function to uncertainties in the surface properties of the cavity is presented.

Acknowledgments

I would first like to thank my academic advisor, Dr. J.R. Mahan, for his help and patience throughout my graduate studies. Under his guidance I have been allowed to grow both as researcher and as an individual.

I would like to thank Dr. Brian Vick and Dr. Kory J. Priestley for their willingness serve on my advisory committee.

I would like to thank my colleagues in Thermal Radiation Group, both at Virginia Tech and at the NASA Langley Research Center: Félix Nevárez, Cristina Sánchez, Katherine Coffey, Edwin Ayala, Amie Smith, Joel Barreto, Stéphanie Weckmann, and Martial Haeffelin. Their generous help and friendship was invaluable in assisting my research.

Finally, I would like to thank my parents, Duane and Joyce, as well as my brothers, Daniel and Jacob, without whose love and support the realization of my goals and aspirations would not have been possible.

Contents

List of Figures

List of Tables

Nomenclature

Symbols:

A	Area (m^2)
C	Capacitance (μF)
cdf	Cumulative distribution function (-)
D	Detectivity (W^{-1})
D^*	Normalized detectivity $(cmHz^{1/2}/W)$
D_{ij}	Distribution factor between surface elements i and j (-)
e_n	Voltage noise density $(nV/Hz^{1/2})$
f	Frequency (Hz)
G_{ij}	Discrete Green's function between surface elements i and j (-)
i	Electric current (A)
i_n	Current noise density $(pA/Hz^{1/2})$
k	Conductivity (W/m^2K)
K	Conductance (Ω^{-1})
N	Noise (V)
pdf	Probability distribution function (-)
P_{AB}	Peltier coefficient (V)
r_s	Specularity ratio (-)
R	Resistance (Ω)
$\Re$	Responsivity (V/W)

S_{AB}	Seebeck coefficient (V)
SNR	Signal-to-noise ratio (-)
t	Time (s)
T	Temperature (K)
V	Voltage (V)
X	Input flux to a radiation detector (W/m^2)
Y	Output signal of a radiation detector (V)

Greek:

α	Absorptivity (-)
δ	Kronecker delta function (-)
λ	Wavelength (μm)
Φ	Incident radiant flux (W/m^2)
σ	Thomson coefficient (V/K)
τ	Time constant (s^{-1})

Subscripts:

e	Electrical
i	Surface element i
j	Surface element j
n	Noise
$p-p$	Peak-to-peak
rms	Root-mean-square
T	Thermal

Chapter 1

Introduction

Increased industrialization over the last century, while bringing a myriad of benefits to society, has greatly impacted the world's social structure and its ecosystem. Pollution of our rivers, oceans, soil, and atmosphere have all increased significantly during this century.

One area of increasing concern is the ongoing pollution of the atmosphere. Continued emissions of CFC's, as well as the burning of fossil fuels, increases the level of CO_2 in the atmosphere and has led to an increased concern over global warming due to the "greenhouse effect."

In order to understand the effects of these changes in our climate system, we must first seek to understand the climate system itself. For example, it is hypothesized that the greenhouse effect causes, through warming of the lower troposphere, increased concentration of water vapor in the atmosphere. Because water is itself a greenhouse gas, this raises the possibility of "runaway" global heating. However, increased water vapor concentration should increase the production of clouds in the atmosphere, which would have an overall cooling effect on the climate.

In an effort to better understand the climate system, the international science community has begun a series of programs aimed at increasing our knowledge and understanding of the

climate through observation of climatic changes and radiation in the atmosphere.

1.1   Description of the instrument

The thermopile linear array detector presented here is a new detector concept developed by Dr. J.R. Mahan of the Department of Mechanical Engineering at Virginia Tech, and Mr. Lawrence W. Langley, president of Vatell Corporation [Mahan and Langley, 1996], intended for use in the Geo-Synchronous Earth Radiation Budget (GERB) instrument.

The thermopile detector consists of a linear array of 256 pixels, or sensing elements. Each pixel is the blackened active junction of a single-junction-pair thermocouple. Each pixel is 60 by 60 μm and is separated from the neighboring pixels by a 3-μm laser-etched gap. The pixels are assumed to be electrically and thermally independent. The geometry of the thermopile detector is given in Figure 1.1 .

Each element of the linear-array detector consists of a blackened active junction and a shielded reference junction. The two junctions are connected electrically by a zinc-antimonide bridge and are connected electrically to the external readout circuits by platinum leads in each junction. The resulting Seebeck coefficient for the zinc-antimonide/platinum thermocouple is many times greater than that of traditional metal/metal thermocouples. The reference junction is in direct thermal contact with an aluminum-nitride substrate, while the active junction is separated from the substrate by a layer of parylene, which acts as a thermal impedance. A complete description of the thermoelectric performance of the thermopile is given by Weckmann [1997].

The detector is bonded to one wall of a wedge-shaped cavity, as shown in Figure 1.2. The walls of the cavity are highly reflective and have a high specularity ratio, defined as the ratio of the specular component of reflectivity to the overall reflectivity. The cavity opens to its surroundings through a 60-μm slit directly above the detector. Collimated light enters through the slit and strikes the detector. Approximately 90 percent of the radiation is

Incident Radiation

Absorber Layer

Zinc-Antimonide Bridge

Reference Junction

Active Junction

Thermal Impedance

Detector Substrate

Not To Scale

(a)

y

z   x

3-μm gap

Detector Substrate

Not To Scale

(b)
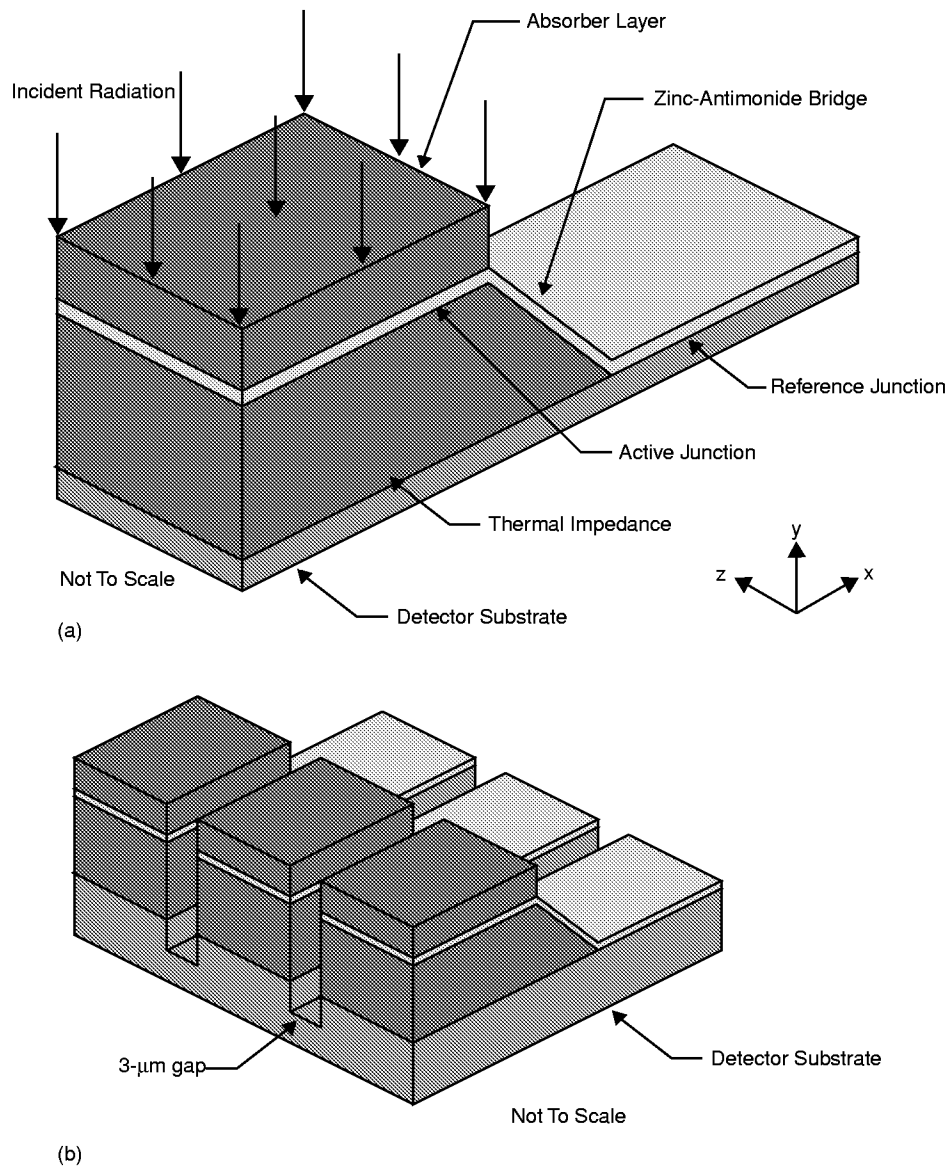
Figure 1.1: Geometry of thermopile detector showing (a) a single element and (b) three of the 256 elements in the proposed linear array

absorbed on direct incidence, with the rest being reflected. However, because of the cavity geometry, most of the reflected radiation returns to be eventually absorbed by the detector. The portion of the radiation that is reflected specularly is absorbed by the pixel to which it was originally incident, while the diffuse portion is generally absorbed by other pixels in the array, thereby creating "optical cross-talk." The elimination of this cross-talk to recover the original data is addressed in this thesis. A complete discussion of the optical behavior of the cavity and detector is given by Sánchez [1998].

1.2   Geo-synchronous Earth Radiation Budget (GERB)

As stated above, long-term measurements of the earth's radiant energy budget are needed to assist with modeling the climate system and predicting long-term trends. These observations need to be satellite based in order to provide sufficient global coverage and sampling. Other satellites that carry radiation budget sensors use polar or other low-earth orbits. Using these orbits, four satellites can provide coverage of the diurnal cycle with a temporal resolution of three hours, which is only marginally adequate. The GERB instrument addresses this undersampling by performing measurements from geo-synchronous orbit. This means that it always observes the same part of the earth but at a continually changing time of the day.

The GERB instrument will measure broadband radiances exiting the Earth from the perspective of the ESA's Meteostat Second Generation (MSG) satellite, with a launch scheduled for the year 2000. The instrument will make both shortwave (0.32–4 μm) and total (0.32–30 μm) measurements, with the longwave (4–30 μm) component determined from the difference between the total and the shortwave. Here "shortwave" refers to the solar spectrum and "longwave" to the Earth-emitted spectrum. Each channel has a sampling time of 300 s. A more complete description of the GERB instrument is given in Table 1.1 [Mueller, 1997].

5
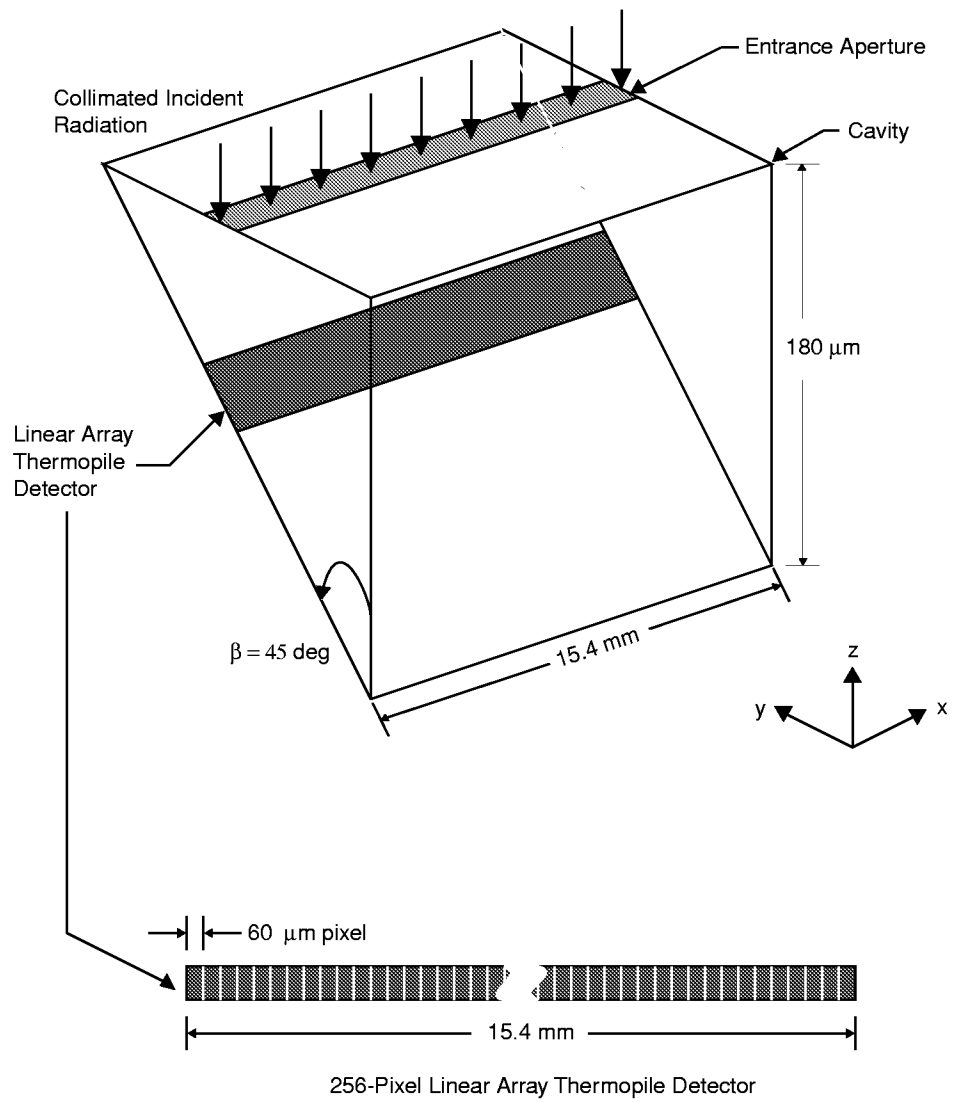
Figure 1.2: Geometry of the cavity showing placement of the linear-array detector

Table 1.1: GERB instrument description [Mueller, 1997]

Platform	Meteostat Second Generation	geo-synchronous (above 0deg, 0deg)
		spin-stabilized (100 rpm)
		launch: 2000
Spectral Bands	shortwave	0.32–4 μm
	total	0.32–30 μm
	longwave	by subtraction
Short-wave filter	quartz	
Accuracy (Target)	shortwave	1 percent
	longwave	0.5 percent
Field of View	43.7 km	at sub-satellite point
Telescope	3-mirror off-axis optics	
	+ 1 fold mirror	(to minimize polarization)
	+ 1 de-spin mirror	(to remove the satellite rotation)
Detector	256 by 1	linear array in North-South direction
Calibration Sources	thermal infrared/solar	blackbody/integrating sphere
Sampling time	300 s	(both channels, complete Earth image)
Mass	less than 30 kg	divided into three "boxes"

1.3 Green's functions

The English mathematician George Green first introduced the idea of potential functions in 1828 [Green, 1828]. In his essay Green describes a system of bodies S and a material point p within the system, and states that the effect, in any given direction, of all the forces acting upon the point, may be described by a function that he calls the "potential function arising from the system S." What Green was describing was the response of the system to an impulse. In the cited paper, Green also introduces what later became known as *Green's functions*. Green introduced these functions in order to solve the differential equation associated with the potential function. Green considered the case where the potential is caused by a single charge at an isolated point such that the Laplace equation is satisfied by the potential function. By assuming that the potential becomes zero on the boundary of the body and increases as $1/r$ as the point charge is approached, Green was able to demonstrate how to solve for the function [Gray, 1994].

Although Green derived his functions to solve problems in electricity and magnetism, the underlying principles of his discovery have been extended for use in many areas of science and engineering. A particular area that makes extensive use of Green's functions is that of conduction heat transfer, as they are particularly well suited to solve the equation of heat diffusion.

Consider the following three-dimensional nonhomogeneous boundary-value problem of heat conduction over region R:

$$\nabla^2 T(r,t) + \frac{1}{k}\, g(r,t) = \frac{1}{\alpha}\frac{\partial T(r,t)}{\partial t},\ t > 0\ , \tag{1.1}$$

with boundary conditions on each surface S_i defined by

$$k_i\,\frac{\partial T}{\partial n_i} + h_i\, T = h_i\, T_{\infty i} \equiv f_i(r,t) \tag{1.2}$$

and the initial condition

$$T(r,t) = F(r),\ t = 0\ . \tag{1.3}$$

Equations 1.1 through 1.3 can be solved by considering the associated Green's function equation over the same region R:

$$\nabla^2 G(r,t|r',\tau) + \frac{1}{k}\delta(r-r')\delta(t-\tau) = \frac{1}{\alpha}\frac{\partial G}{\partial t}, \ t > 0 \ , \tag{1.4}$$

with the homogeneous boundary condition

$$k_i \frac{\partial G}{\partial n_i} + h_i G = 0, \ t > \tau \ . \tag{1.5}$$

The solution to Equation 1.1 subject to Equations 1.2 and 1.3 is

$$
\begin{aligned}
T(r,t) =& \int_R G(r,t|r',\tau)|_{\tau=0} F(r')\, dv' \\
&+ \frac{\alpha}{k}\int_{\tau=0}^{t} d\tau \int_R G(r,t|r',\tau)\, g(r',\tau)\, dv' \\
&+ \alpha \int_{\tau=0}^{t} d\tau \sum_{i=1}^{N} \int_{S_i} G(r,t|r',\tau)|_{r'=r_i} \frac{1}{k_i} f_i(r',\tau)\, ds_i' \ ,
\end{aligned}
\tag{1.6}
$$

where dv' and ds_i' are differential volume and surface elements, respectively.

The physical significance of the Green's function $G(r,t|r',\tau)$ for the three-dimensional problem is as follows: It represents the temperature at the location r, at time t, due to an instantaneous point source of unit strength, located at the point r', releasing its energy at time $t = \tau$ [Özişik, 1993]. This definition again illustrates that the Green's function G represents the effect at (r,t) to an impulsive point source at (r',τ).

While the Green's functions have been used extensively in conduction heat transfer, and to some degree in convective heat transfer, their use in radiation heat transfer has remained relatively rare. Sharma and Cogley [1982] have developed an approach to solving radiative heat transfer problems with scattering in a non-gray, plane-parallel environment, using scattering functions (Green's functions).

With the advent of faster computers, numerical methods of radiation heat transfer analysis, such as the Monte-Carlo ray-trace (MCRT) method, make possible a new area of application of Green's functions. Mahan et al. [1998] have proposed the use of a discrete Green's function to represent the scattering in a cavity based on the distribution factor in the MCRT method.

1.4 Goals and motivation

The Thermal Radiation Group, under the guidance of Dr. J.R. Mahan of the Department of Mechanical Engineering at Virginia Polytechnic Institute and State University, has been involved in the development of optical, radiative, thermal conduction and electronic models of spaceborne radiometers for the last twenty-five years. Design and analysis efforts include NASA's ERBE and CERES instruments.

Over the last three years, the Thermal Radiation Group has been involved in an effort to develop a new technology of thermal radiation detectors for use in the next generation of spaceborne instruments, including possible use on geo-synchronous earth radiation budget (GERB) applications. The technology development has consisted of two major efforts:

- development of optical and electrothermal numerical models to predict the detector's physical behavior and to aid in the design of the optimal configuration

- fabrication and testing of actual prototype detectors.

Towards these ends, a dynamic electrothermal model of the detector was developed by Weckmann [1997], an optical model of the detector cavity was developed by Sánchez [1998], and an experimental procedure was developed by Barreto [1998] to estimate the electrothermal properties of the detector.

The aims of the current research include:

- integration of the previous optical and electrothermal models into an end-to-end model of the cavity and detector to accurately model and predict the performance of the instrument

- development of a method to recover the incident radiation that has been spread through the cavity via reflections, by use of discrete Green's functions that characterize the

scattering of radiant energy due to the cavity effect, as well as performing a parametric study of the behavior of the discrete Green's functions with variations in the physical parameters of the cavity

- testing and characterization of actual physical prototypes of the thermopile radiation detectors to determine the actual performance of the detectors.

A FORTRAN program, **Detector.f**, is developed to achieve the numerical modeling aims listed above. All physical testing of the detectors was performed at the NASA Langley Research Center in Hampton, Virginia.

Chapter 2

Radiation Detectors

This chapter attempts to provide the reader with a brief overview of radiation detectors, and particularly thermal detectors. Topics include general properties of detectors, including responsivity, signal-to-noise ratio (SNR), fundamental noise, etc. The different types of thermal detectors are discussed, with particular attention paid to thermopile detectors. It should be noted that this chapter is not meant to be an exhaustive discussion of these topics, but rather an introduction to several topics that will arise in later chapters. A large portion of this chapter was adapted from material by Lenoble [1993] and Haeffelin [1997].

2.1 General properties of radiation detectors

The input signal, or flux, to a filtered radiation detector is

$$X(\lambda) = \alpha_\lambda(\lambda) \, \Phi_\lambda(\lambda) \,, \tag{2.1}$$

where $\Phi_\lambda(\lambda)$ is the incident monochromatic radiant flux and $\alpha_\lambda(\lambda)$ is the monochromatic absorptivity of the detector surface at a particular wavelength λ.

The absorptivity of the detector can be enhanced by two means. The first is through the use

of a "black" coating with a high absorptivity on the detector surface. The second is through a cavity, which causes the incident flux to strike the detector surface multiple times through specular (mirror-like) reflections.

There are two major categories of radiation detectors: thermal detectors and photon detectors. Thermal detectors transform the absorbed radiant energy into sensible heat, producing a temperature difference that can be directly measured, or that can be used to induce an electromotive force, or emf. In photon detectors, each photon in the absorbed radiant energy is used to excite an electron in the detector material, thereby increasing the energy level of the electron. If the energy of the electron is raised sufficiently to cause the electron to jump to a higher energy level, the electron is extracted from the detector, producing a measurable photoelectric current.

The $responsivity$ of the detector is defined as the signal output per unit of incident energy, and is represented by

$$\Re = \frac{Y}{\Phi} = \alpha \frac{Y}{X} \, , \tag{2.2}$$

where Y is the output yielded by the detector.

The output of the detector always contains a certain amount of noise. A portion of this noise arises from the measurement procedure and can be minimized. The remainder is noise that is inherent to the physical properties of the detector, and is known as $fundamental\ noise$. The output signal of the detector can be expressed as the root-mean-square (rms) value $\langle Y \rangle$ defined

$$\langle Y \rangle = \frac{1}{n} \sum_{i=1}^{n} Y_i \, , \tag{2.3}$$

and the noise is expressed as the rms noise $(\langle \Delta Y^2 \rangle)^{1/2}$ defined

$$N = (\langle \Delta Y^2 \rangle)^{1/2} = \left[\frac{1}{n} \sum_{i=1}^{n} (Y_i - \langle Y \rangle)^2 \right]^{1/2} \, . \tag{2.4}$$

The *signal-to-noise ratio* is defined

$$SNR = \frac{\langle Y \rangle}{(\langle \Delta Y^2 \rangle)^{1/2}} \; . \tag{2.5}$$

The *noise equivalent power* (NEP) is the detector input that produces a $SNR = 1$, and the *detectivity* is given by

$$D = \frac{1}{NEP} \; . \tag{2.6}$$

Detector responsivity is typically wavelength dependent, but different detectors can be characterized using the *normalized detectivity*

$$D^* = D \, (A \, \Delta f)^{1/2} \; , \tag{2.7}$$

with A being the sensitive area of the detector and Δf the measurement bandwidth.

2.2   Fundamental noise of radiation detectors

Three types of noise act as fundamental limits on the performance of radiation detectors: shot noise, Johnson noise, and temperature noise.

2.2.1   Shot noise

Shot noise arises due to the granular structure of the material from which the element is manufactured, and affects both the incident radiation and the electrical output of the detector. The radiant flux is composed of a beam of n photons striking the detector per unit of time, and the electric current density is due to the transport of n electrons per unit time. Any measurement procedure of these quantities actually consists of counting n_t discrete events in a time interval Δt, the probability of occurrence of which can be represented by a Poisson distribution.

The average current observed per unit of time is

$$\langle i \rangle = \frac{\langle n_t \rangle e}{\Delta t} \ , \tag{2.8}$$

where e is the electron charge of the particle, and the current fluctuation is given by

$$\langle \Delta i^2 \rangle = \langle (i_t - \langle i \rangle)^2 \rangle \ . \tag{2.9}$$

Equation 2.9 can be represented in the frequency domain as

$$\langle \Delta i^2 \rangle = 2\,e\,\langle i \rangle\,\Delta f \ , \tag{2.10}$$

with Δf representing the frequency bandwidth. The voltage fluctuation over a resistor R is given by

$$\langle \Delta V^2 \rangle = 2\,R\,e\,\langle V \rangle\,\Delta f \ . \tag{2.11}$$

Photons differ from electrons in that the photon energy $h\nu$ varies with frequency ν and the radiant energy. For high frequencies ($\lambda < 40\ \mu m$) the noise fluctuation is

$$\langle \Delta n_t^2 \rangle = \langle n_t \rangle \left[1 + \frac{1}{\exp(h\nu\,/\,kT) - 1} \right] \tag{2.12}$$

for photons of frequency $\nu = c/\lambda$, where c is the speed of light in the medium, h is the Planck constant, and k is the Boltzmann constant. For low frequencies ($\lambda > 40\ \mu m$) the noise fluctuation is

$$\langle \Delta n_t^2 \rangle = \langle n_t \rangle \left[1 + \frac{kT}{h\nu} \right] \ . \tag{2.13}$$

The corresponding fluctuation in the incident energy is

$$\langle \Delta w^2 \rangle = \langle \Delta n_t^2 \rangle\,(h\nu)^2 = \langle \Delta n_t \rangle\,h\nu kT \ , \tag{2.14}$$

and is known as *thermal noise* (J^2). At short wavelengths the noise due to radiation is dominant, and at long wavelengths it is not.

2.2.2 Johnson noise

Johnson noise is the noise associated with random thermal motion within the resistance of the detector. These fluctuations can be regarded as being due to an electromotive force, e_f, at a frequency f. For a small frequency interval, Δf, these fluctuations are given by

$$\langle e_f^2 \rangle = E\Delta f \ . \tag{2.15}$$

The constant E has been found to be represented by $E = 4kTR$, where k is the Boltzmann constant and R is the electrical resistance of the detector. Equation 2.15 can therefore be written

$$\langle e_f^2 \rangle = 4kTR\Delta f \ . \tag{2.16}$$

2.2.3 Temperature noise

The temperature of a thermal detector fluctuates randomly around a mean value, due to heat transfer between the detector and its surroundings. These fluctuations, called temperature noise, are expressed by

$$\langle \Delta T^2 \rangle = \frac{kT^2}{C_T} \ , \tag{2.17}$$

where C_T is the thermal capacitance of the detector. The fluctuation of radiant power is given by

$$\langle \Delta X_f^2 \rangle = 4kT^2 K_T \Delta f \ , \tag{2.18}$$

where K_T is the thermal conductance $(1/R_T)$ of the detector.

2.3 Thermal detectors

The output signal, Y, of a thermal detector is induced by a temperature variation ΔT caused by the absorbed flux. The responsivity of the thermal detector can be expressed as

$$\Re = \alpha \frac{\Delta T}{X} \frac{Y}{\Delta T} \, . \tag{2.19}$$

The factor $\Delta T / X$ is a physical property that depends only on the thermal characteristics of the detector.

If the temperature of the detector is raised by ΔT_o and then allowed to decay without any external energy source present, the exponential temperature decay is given by

$$\Delta T = \Delta T_o \, \exp\left[-\frac{t}{\tau}\right] \, , \tag{2.20}$$

where $\tau = C_T \, R_T$ is the thermal time constant of the detector. A smaller time constant allows the system to return to equilibrium more rapidly and results in a "quicker" detector response.

If the detector is irradiated with an incident flux X modulated at a frequency f such that

$$X = X_f \, \exp\left(2\,\pi\,j\,f\,t\right) \, , \tag{2.21}$$

where j is the imaginary operator, $\sqrt{-1}$, then the temperature difference ΔT is modulated at the same frequency such that

$$\Delta T = \Delta T_f \, \exp\left(2\,\pi\,j\,f\,t\right) \, , \tag{2.22}$$

where

$$\Delta T_f = \frac{X_f}{K_T \, (1 + 4\,\pi^2 \, f^2 \, \tau_T^2)^{1/2}} \, . \tag{2.23}$$

At higher frequencies, ΔT_f falls off as $1/f$. The maximum operating frequency, f_m, is defined as

$$f_m = \frac{1}{2\,\pi\,\tau_T} \, . \tag{2.24}$$

2.3.1 Thermopiles

Thermopiles operate on the thermoelectric principles on which thermocouples are based. The three thermoelectric effects that influence the behavior of the thermocouple are the Peltier, Seebeck and Thomson effects [Pollock, 1985].

The Seebeck effect, named for German scientist Thomas Johann Seebeck, states that an electric current will flow in a closed circuit composed of two dissimilar metals if their junctions are maintained at different temperatures. If the circuit is open, an electromotive force, E_{AB} is created. This force, termed the relative Seebeck voltage, is directly proportional to the temperature difference ΔT between the two junctions,

$$E_{AB} = S_{AB}\,\Delta T \,, \qquad (2.25)$$

where S_{AB} (V/K) is the Seebeck coefficient.

The Peltier effect, named for French physicist Jean Charles Peltier, states that when an electric current flows across a junction of two dissimilar metals, heat is liberated or absorbed, depending on the direction of the current flow relative to the Seebeck voltage associated with the junction. The power liberated or absorbed is given by

$$P = P_{AB}\,i \,, \qquad (2.26)$$

where i is the electric current and P_{AB} (V) is the relative Peltier coefficient.

The Thomson effect is due to an electric current flowing through a conductor in which exists a temperature gradient. Heat is liberated if the current flow direction coincides with the direction of heat flow, otherwise it is absorbed. The power liberated or absorbed is given by

$$P = \sigma(T)\,i\,\frac{\partial T}{\partial x} \,, \qquad (2.27)$$

where $\partial T/\partial x$ is the temperature gradient along the conductor and $\sigma(T)$ (V/K) is the Thomson coefficient.

The relationship among Equation 2.25, Equation 2.26, and Equation 2.27 was developed by Pollock [1985]. Pollock states that "the Seebeck effect is the result of both the Peltier and Thomson effects." The relationship between the three effects is

$$\frac{\partial E_{AB}}{\partial T} = \frac{\partial P_{AB}}{\partial T} + (\sigma_B - \sigma_B) \ . \tag{2.28}$$

For a more thorough treatment of the thermoelectric and thermodynamic properties of thermopiles, the reader is referred to Weckmann [1997].

When used as thermal radiation detectors, one junction of the thermocouple is maintained at a reference temperature equal to the ambient temperature, T_∞, while the other junction is typically coated with a black absorber material and allowed to store thermal energy by absorbing incident radiation. A thermopile consists of several thermocouples connected in series to increase the emf output. For n junction pairs, the output signal is

$$Y = \Delta V = n\, S_{AB}\, \Delta T \ . \tag{2.29}$$

Huang [1990] presents a formal development of Equation 2.29 as well as excellent methods for calibration and signal conversion of thermopiles for temperature measurements.

The responsivity of a thermopile detector is

$$\Re = \frac{\alpha\, n\, S_{AB}}{K_T\, (1 + 4\,\pi^2\, f^2\, \tau_T^2)^{1/2}}\ (V/W) \ , \tag{2.30}$$

which, at low frequencies, reduces to

$$\Re = \frac{\alpha\, n\, S_{AB}}{K_T}\ (V/W) \ . \tag{2.31}$$

2.3.2   Bolometers

In a bolometer a temperature increase ΔT due to absorbed heat flux produces a change in the resistance R_o of the detector according to

$$\Delta R = R - R_o = R_o\, P\, \Delta T \ , \tag{2.32}$$
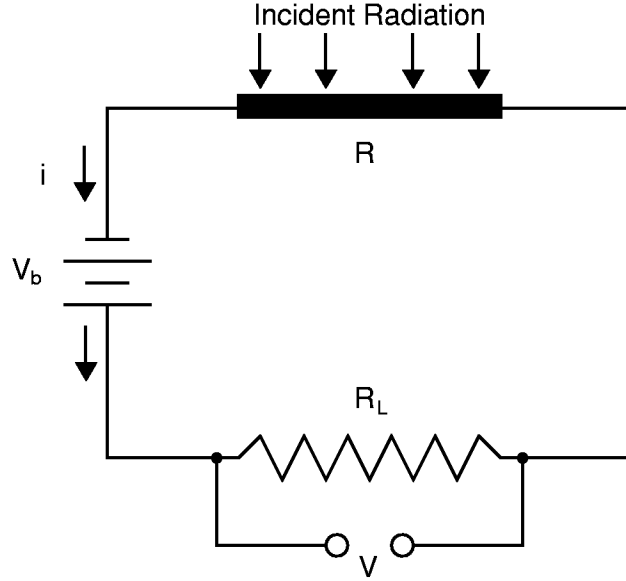
Figure 2.1: Schematic diagram of a typical bolometer circuit (adapted from Lenoble [1993])

where P (K^{-1}) is the temperature coefficient of the resistance. If the bolometer is connected in series with a voltage source, V_b, and a resistance R_L much larger than R_o, as seen in Figure 2.1, the voltage V across R_L varies with the temperature according to

$$\Delta V = \frac{V_b R_o P \Delta T}{R_L} \, . \tag{2.33}$$

The voltage difference ΔV is equivalent to the output Y, and thus the responsivity can be written as

$$\Re = \frac{V_b R_o P}{R_L K_T (1 + 4 \pi^2 f^2 \tau_T^2)^{1/2}} \; (V/W) \, , \tag{2.34}$$

or at low frequencies

$$\Re = \frac{V_b R_o P}{R_L K_T} \; (V/W) \, . \tag{2.35}$$

2.3.3 Pyroelectric detectors

A pyroelectric detector consists of a plate of a crystal that, when heated by absorbed radiant flux, produces electric charges on opposite sides of the plate due to a change in average

position of the electrons in the crystal. This leads to a current in an external circuit if the input signal is modulated, as a pyroelectric detector does not respond to an unmodulated signal. This is because the initial charge separation drains off through the electrical resistance of the crystal material.

The responsivity of a pyroelectric detector with equivalent electric resistance and capacitance of R_e and C_e, respectively, is given by

$$\Re = \frac{\alpha \, 2\pi \, f \, P_T \, A \, R_e}{K_T \, (1 + 4\,\pi^2 \, f^2 \, \tau_T^2)^{1/2} \, (1 + 4\,\pi^2 \, f^2 \, \tau_e^2)^{1/2}} \; (V/W) \,, \qquad (2.36)$$

where A is the sensitive detector area, P_T is the pyroelectric coefficient, and $\tau_e = C_e \, R_e$ is the electrical time constant.

A frequency range, $f \ll 1/2\pi\tau_e$ and $f \gg 1/2\pi\tau_t$ exists where the responsivity does not depend on the modulation frequency. Pyroelectric detectors are typically operated in this frequency range. The responsivity in this frequency range is

$$\Re = \frac{\alpha \, P_T \, A \, R_e}{K_T \, \tau_T} = \frac{\alpha \, P_T \, A \, R_e}{C_T} \; (V/W) \,. \qquad (2.37)$$

2.4   Thermopile materials

The following is a brief overview of some of the materials used in thermopile detectors. The two areas discussed are materials used in the thermocouple junctions and absorber layers, and some of the issues and current technology associated with each.

2.4.1   Thermocouple junctions

Two types of thermocouple junction are considered: two thin metal layers, and a thin metal layer with a semiconductor material layer.

An example of a typical thermocouple junction consisting of two thin metal layers is a

bismuth-antimony, Bi-Sb, thermocouple. A typical Bi-Sb thermocouple junction has a Seebeck coefficient of approximately 100 $\mu V/K$ [Lenoble, 1993].

Recent technological and manufacturing advances have seen an increased use of silicon-based thermopile technology. The advantages of using silicon in thermopiles include its compatibility with CMOS-standard processes, which results in higher reliability and less variation between production runs, and its increased stability with temperature [Schmidt, 1995]. Another major advantage of silicon-based thermocouples is the ability to alter the doping concentration in the material to change the resistivity and thermoelectric power, and can be optimized for higher sensitivity/noise ratios. Properly doped silicon can have a Seebeck coefficient as high as 1 mV/K, although standard fabrication processes typically produce a Seebeck coefficient on the order of 100 $\mu V/K$ [Foote et al., 1998].

Recently, new combinations of semiconductor/metal combinations have been under investigation with the aim of increasing thermopile performance. A thermopile detector comprised of zinc-antimony (Zn-Sb) and platinum (Pb) with a Seebeck coefficient of 920 $\mu V/K$ [Krieder, 1994] and a broadband sensitivity of 0.088 $\mu V/W/m^2$ [Mahan et al., 1998] has been reported. Foote et al. [1998] have reported arrays of thermopile detectors comprised of alternating lines of Bi-Te and Bi-Sb-Te with reported response times of 99 ms, zero-frequency D^* values of 1.4×10^9 $cm\,Hz^{1/2}/W$ and responsivity values of 1100 V/W when viewing a 1000 K blackbody source. These values represent the best published performance of a thermopile array to date.

2.4.2   Thermopile absorber layers

The absorber layer coating the hot junction of the thermopile is an essential component in the overall performance of the thermopile detector. The absorptivity must be high for increased sensitivity, but the mass of the absorber layer must be small for a shorter thermal time constant. The deposition of the absorber layer plays a critical role in the development of thermopile technology.

Three primary methods are available for the deposition of the absorber layer on the thermopile [Lang et al., 1991] :

- Thin metallic films. For thick metallic films, the high mobility of electrons in the material causes reflection of incident radiation. Conversely, very thin metal films do not provide sufficient electrons to interact with the incident light, making the film transparent to incident radiation. A critical intermediary thickness exists for which the electrons can interact but not move, and thus are able to absorb incident photons. A broadband absorption of 0.5 in a very narrow range of film thickness has been reported.

- Highly porous platinum black deposited by a galvanic process. If platinum is deposited by electroplating, and a small amount of a heavy metal, such as lead, is added, the result is a porous film called "platinum black". A film of 1.5 mg/cm^2 provides an absorptivity of approximately 0.95 at $\lambda = 10 \, \mu m$.

- Evaporation of a metal in an atmosphere of low-pressure nitrogen. A common procedure for adding a porous absorbing layer is the evaporation of gold in a nitrogen atmosphere. The resulting layer is called "gold black." This process is the best of the three, providing an absorptivity of approximately 0.95 at $\lambda = 10 \, \mu m$ with a film of 250 $\mu g/cm^2$.

Some promising "off-the-shelf" coatings include Chemglaze Z-306, ECP-2200, and DeSoto Black. When mixed with an additive such as carbon black, these materials exhibit a reflectance of less than 10 percent over a wide spectral range [Smith and Howitt, 1986].

Chapter 3

Testing and Characterization of a Thermopile Radiation Detector

3.1 Design of an output signal amplifier

As series of prototype detectors was fabricated by the Vatell Corporation and submitted to the NASA Langley Research Center for evaluation. Output of these prototype detectors, viewing a simulated blackbody at 1100K, was in the range of 50 nV to 50 μV, depending on the wavelength band being observed. Available instruments used to read the signal have a least count on the order of 1 mV; therefore, the detector output had to be amplified for accurate measurements to be taken.

The design of an appropriate pre-amplifier for this application involved several considerations. The first of these was determining the gain required to give a measurable signal. A gain of 50,000 was decided upon, giving an optical broadband output of approximately 1.5 V and an optically filtered output of 1-100 mV, depending on the bandpass of the optical filters used. The next consideration in the design process was determination of the type of amplifier circuit to be used as well as selection of appropriate operational amplifiers (op-
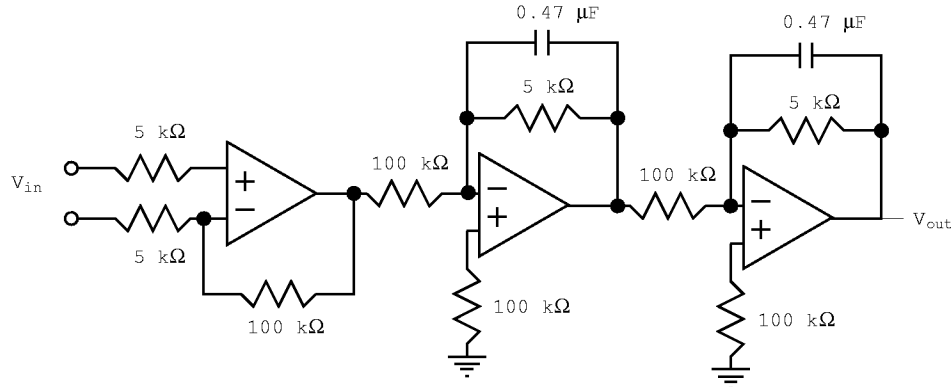
Figure 3.1: Schematic circuit diagram of output pre-amplifier

amps). After several different designs were considered, a multi-stage differential design was chosen as being the most appropriate for this application. The first stage of the pre-amplifier is a differential stage with a gain of 20, followed by two identical inverting stages with gains of 50 each. Once the circuit had been designed, an appropriate op-amp had to be chosen. The main consideration in selecting the op-amp is that it be low-noise. This was extremely important in this case due to the small amplitude of the detector output signal. Anything more than a few millivolts of noise from the amplifier would tend to drown out the detector signal and cause a poor signal-to-noise ratio. Several different op-amps were considered and tested, and while some had better listed characteristics, the Harris HA-5127 [Harris Semiconductors, 1993] had the best performance when tested under laboratory conditions. A schematic diagram of the final circuit is given in Figure 3.1 .

The frequency response of the pre-amplifier was tested by attaching the input of the pre-amplifier to a voltage source of 200 μV and varying the frequency of the source. The output voltage was recorded and the gain calculated for each frequency value. The 3-dB down point was found to be approximately 100 Hz. The frequency response characteristics are given in Figure 3.2.
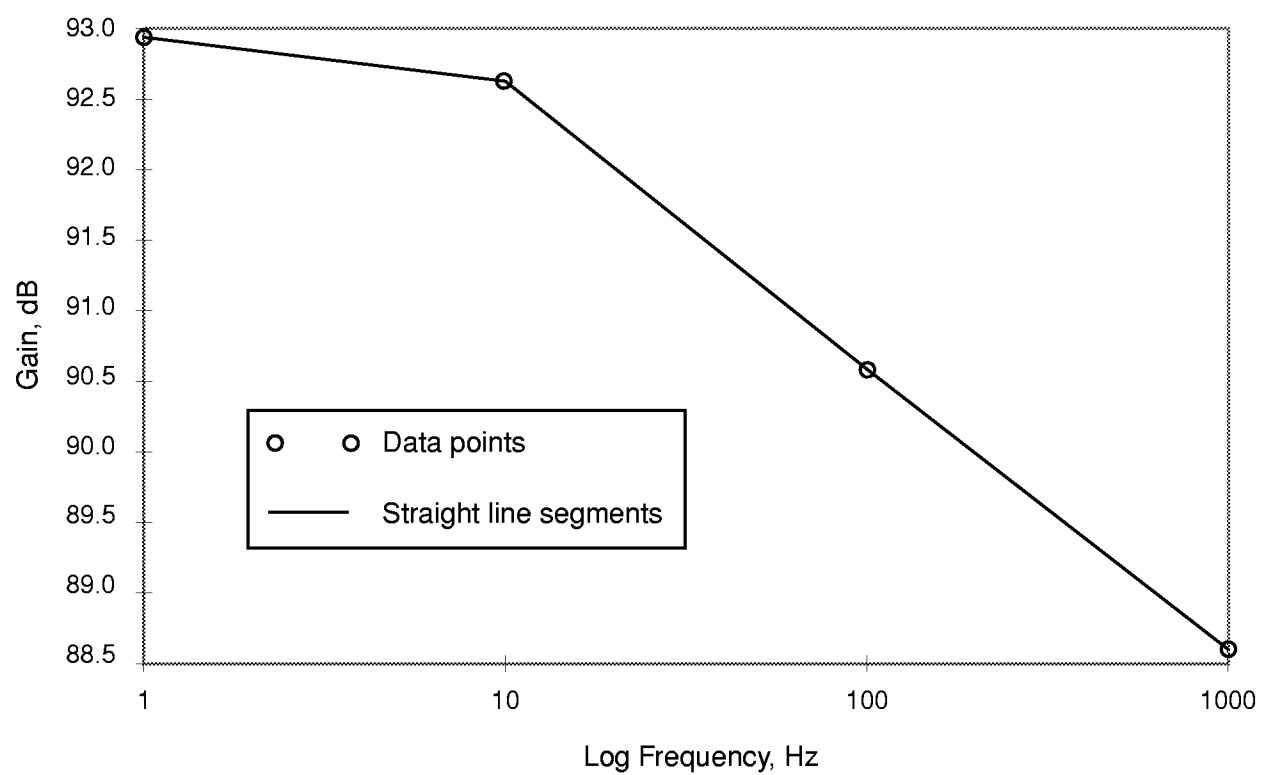
Figure 3.2: Measured frequency response of output pre-amplifier

3.1.1 Noise analysis of output pre-amplifier

A noise analysis of the final amplifier circuit was performed to predict the total level of noise that the circuit would contribute to the signal. The sources of noise that were considered were voltage and current noise inherent to the op-amps, and Johnson noise, which is thermal noise caused by heating of the resistors as current is passed through them. Several other possible sources of noise exist, but were considered negligible. Due to the nature of a multi-stage amplifier, noise from the first stage of the amplifier will tend to be the dominant noise source. This is because feedback in the second and third stages can at least theoretically reduce noise in these stages to negligible levels.

The voltage noise is given by

$$N_v = e_n(1 + G) \ , \tag{3.1}$$

where e_n is the voltage noise density of the op-amp and G is the gain of the first stage of the pre-amplifier. The current noise of the non-inverting terminal of the op-amp is given by

$$N_{i,+} = i_n R_{(+)}(1 + G) \ , \tag{3.2}$$

where i_n is the current noise density of the op-amp and $R_{(+)}$ is the electrical resistance seen at the non-inverting terminal of the op-amp. Similarly, the current noise of the inverting terminal is given by

$$N_{i,-} = i_n R_{(-)}(1 + G) \ , \tag{3.3}$$

where $R_{(-)}$ is the electrical resistance seen at the inverting terminal of the op-amp. The Johnson noise of each resistor in the first stage is given by

$$R_n = (4kTR)^{\frac{1}{2}} \ , \tag{3.4}$$

where k is the thermal conductivity, T is the temperature, and R is the electrical resistance of each resistor.

The specified values of the voltage noise density, e_n, and the current noise density, i_n, for the HA-5127 Op-Amp are 3.8 $nV/\sqrt{Hz}$ at 100 Hz and 1.7 $pA/\sqrt{Hz}$ at 100 Hz, respectively [Harris Semiconductors, 1993].

The calculated noise from the first stage is 3 μV, and the calculated total noise for the amplifier is 7 mV. Subsequent testing of the actual amplifier showed a noise contribution from the amplifier of approximately 20 mV, roughly three times the predicted value.

3.2   Testing of the detectors

The prototype detector provided for testing consisted of five separate detectors aligned in a linear array. We were interested in testing for three parameters of these detectors: electrical resistance, sensitivity, and spectral response. Specifically, we were not interested in testing the dynamic response of these prototypes because they were much larger than the practical linear-array detectors. It should be noted that in all ensuing discussions, responsivity refers to the output of the detector per unit of radiant power seen by the detector, while sensitivity refers to the output of the detector per unit of radiant flux seen by the detector. Of course, the sensitivity can be calculated from the responsivity if the area of the detector visible to the radiant power is known.

The electrical resistance of the detectors was an important parameter to determine, both because of its effect on the amplifier circuit and to better understand the behavior of the detectors. This is because a change in electrical resistance with time might imply other changes in the properties of the detector. Two tests were utilized to measure the electrical resistance of the detectors. The first test involved attaching the positive and negative terminals of each detector to a Hewlett-Packard 4285A Precision LCR Meter. Measurements were taken with the meter set to a bias of -0.5, 0, 0.5V, and the measurements were averaged over the three settings. The second test consisted of using a Hewlett-Packard 4142B Modular DC Source Monitor and a METRICS software package. The monitor set a voltage and measured the

resultant current across each detector. The software plotted the voltage against current, and the slope of the resulting linear fit of the data points gave the electrical resistance of the detectors. Results of both tests are given in Table 3.1.

Table 3.1: Electrical resistance of detectors tested

Detector	Electrical resistance, kΩ LCR Meter	Electrical resistance, kΩ DC Monitor and METRICS
1	24.0	24.12
2	9.4	9.05
3	5.4	5.31
4	20.9	20.92
5	20.9	20.13

The next parameter of interest was the sensitivity of the detectors. Sensitivity is defined as the voltage produced by the detector per unit of flux incident upon the detector. The sensitivity of the detectors was tested first with a broadband source, and then with the same source viewed through a series of optical filters, to determine if the sensitivity of the detectors remained constant over different wavelength bands of incident radiation.

A benchmark measurement was needed for calibration. This was accomplished using a reference detector. A reference detector is typically a similar type of detector with a known responsivity or sensitivity. If the two detectors are illuminated with the same amount of radiation, then the ratios of the output signals should be the same as the ratios of the sensitivities, and from this the sensitivity of the detector of interest can be calculated.

The detector used as the reference detector was the Oriel IR Pyroelectric Detector, Model 70124. The responsivity of the detector was 1000 V_{rms}/W and 1920 V_{p-p}/W.

The test set-up shown in Figure 3.3 was used to test the sensitivity of the detectors. The Mikron Blackbody Calibration Source was used as the radiation source for the tests. The detector was mounted on an x-y positioning table, positioned such that it lay on the optical
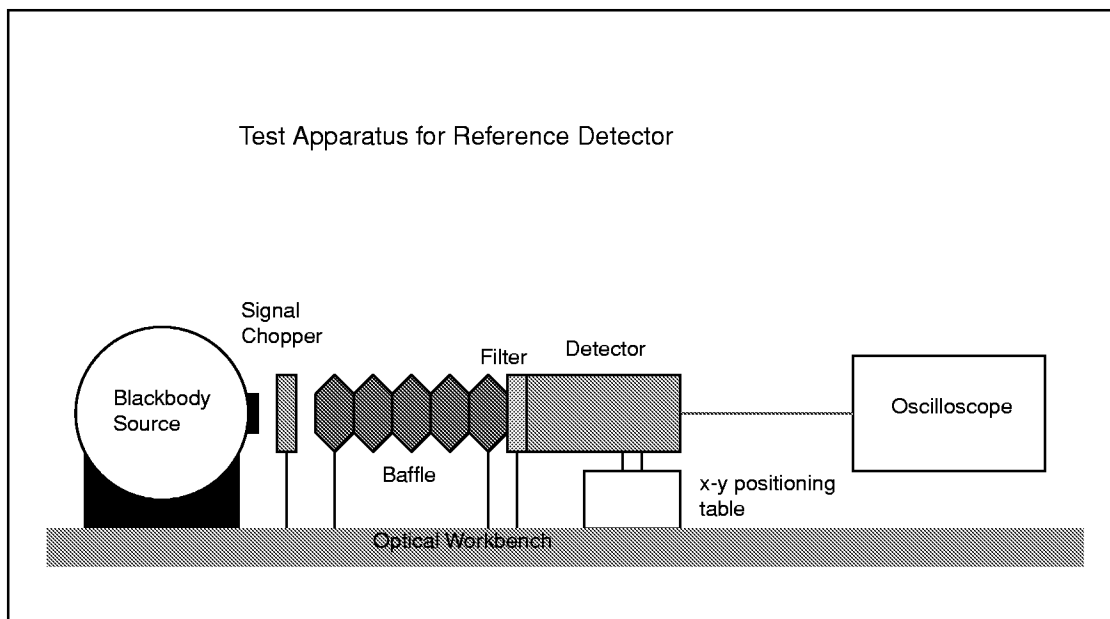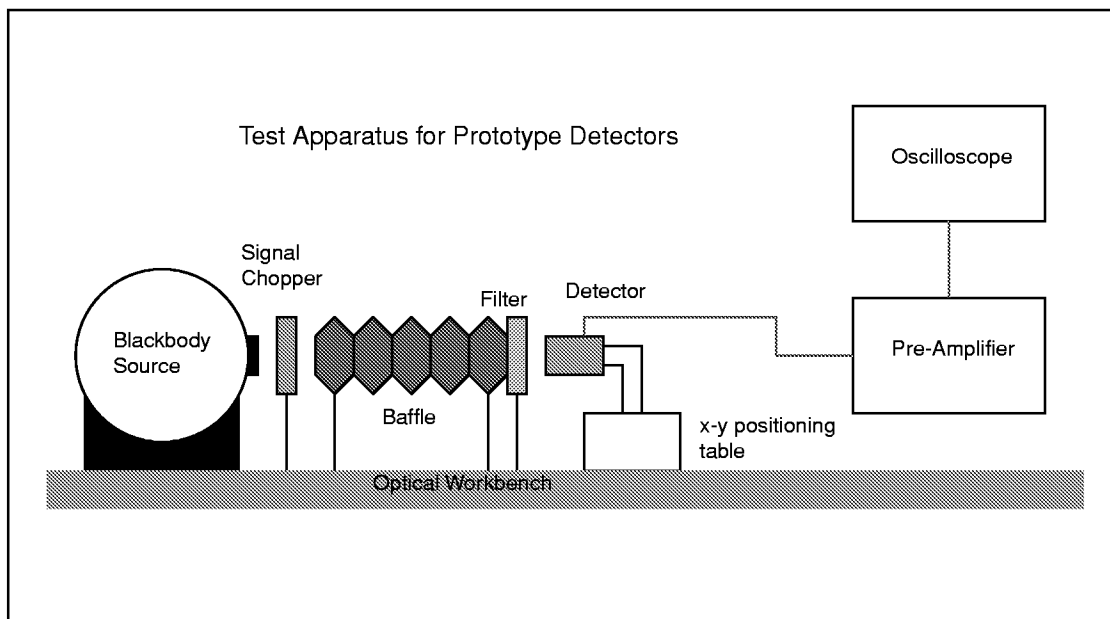
Figure 3.3: Schematic diagram of testing apparatus

axis of the blackbody. The detector surface was mounted perpendicular to and facing the source. To ensure that the reference and prototype detectors were positioned in the same place with a high degree of repeatability, the focal-plane method was used. A kinematic mount was placed in a permanent position in front of and facing the detector with a removable microscope objective attached to the mount. The axial position of the detector was adjusted until it lay in the focal plane of the objective. This gave repeatable position with 100 μm precision. The reference scans were taken with a signal chopper in front of the source set at 134 Hz, and the output of the Oriel detector running directly into the oscilloscope. The prototype detectors were tested with a shutter in front of the source set at 1 Hz, and with the output of the detector connected to the input of the pre-amplifier described in the previous section, whose output was displayed by an oscilloscope. The prototype and reference detectors were tested with no filters, and with three separate filters of different passbands. The results of these tests are given in Table 3.2.

Using a responsivity of the reference detector of 1920 V_{p-p}/W and an area of 19.6 mm^2, and by assuming that the prototype detectors see the same flux as the reference detector, we can calculate the sensitivity of the prototype detectors. These results are given in Table 3.3. The measured values for broadband sensitivity agree well with the value predicted by the end-to-end model of the detector of 870 $V/W/cm^2$.

The spectral response of the sensitivity of the two detectors over a wavelength interval $2 \leq \lambda \leq 12$ μm is shown graphically in Figure 3.4. The sensitivity of each detector decreases as the wavelength increases. This is most likely due to decreased absorptivity of the absorber coating at longer wavelengths [Smith and Howitt, 1986].
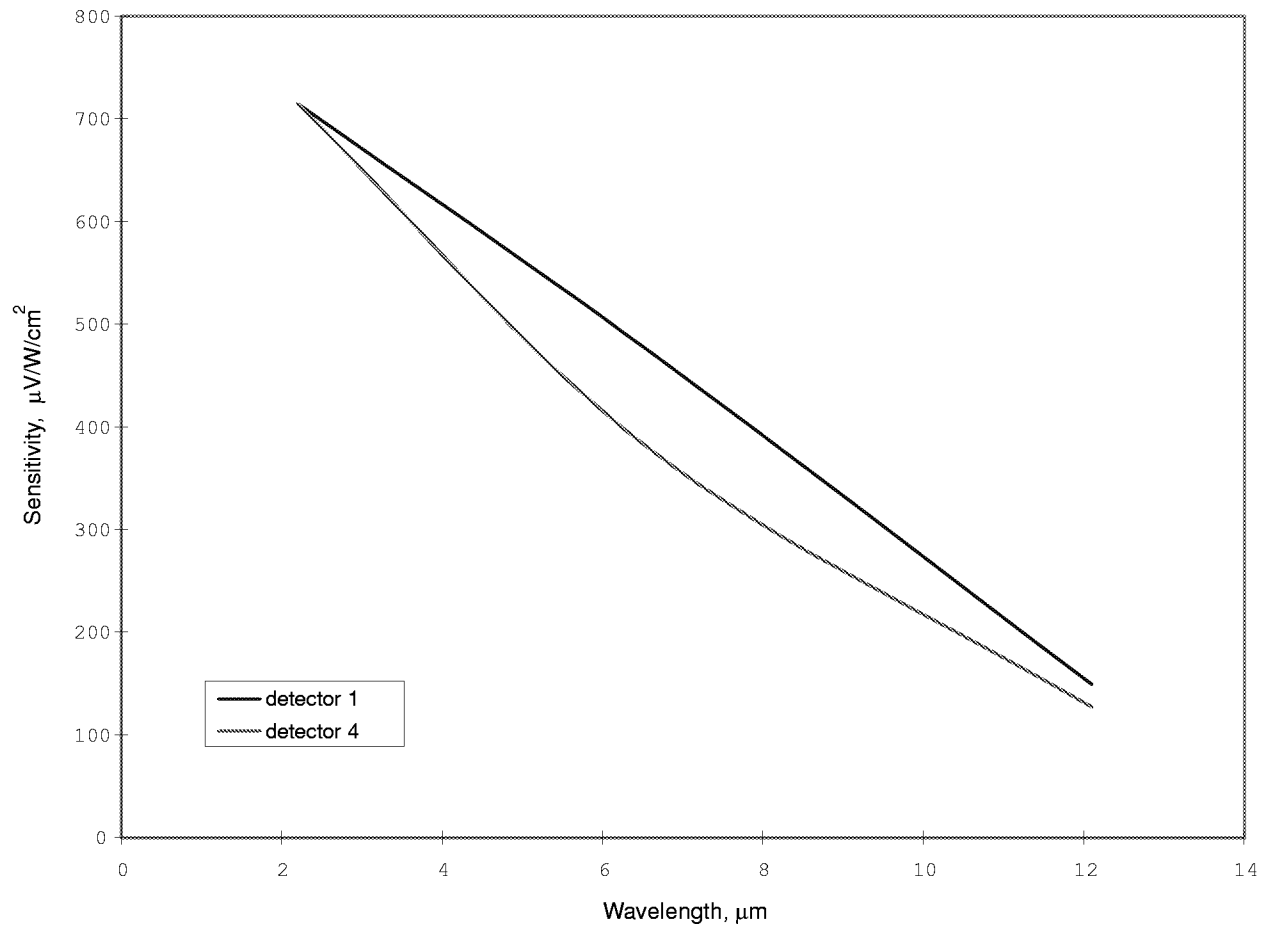
Figure 3.4: Spectral response of the sensitivity of two prototype thermopile detectors

Table 3.2: Signal output for testing of two thermopile detectors

	Mean signal	Standard deviation
No filter		
Detector 1	1.39 V	0.015 V
Detector 4	1.44 V	0.042 V
Oriel Detector	13.85 V	0.079 V
Filter K, 2.0-2.4 μm		
Detector 1	86 mV	4.4 mV
Detector 4	86 mV	6.1 mV
Oriel Detector	1.02 V	0.018 V
Filter B, 6.548-6.708 μm		
Detector 1	11 mV	1.2 mV
Detector 4	8.78 mV	3.7 mV
Oriel Detector	197 mV	0.500 mV
Filter K, 11.55-12.65 μm		
Detector 1	2.0 mV	0.25 mV
Detector 4	1.7 mV	0.13 mV
Oriel Detector	114 mV	2.21 mV

Table 3.3: Sensitivity values for two prototype thermopile detectors

| Wavelength range, μm	Detector 1, $\mu V/W/cm^2$	Detector 4, $\mu V/W/cm^2$
Broadband	852	882
2.0-2.4	715	715
6.548-6.708	474	379
11.55-12.65	149	127

Chapter 4

Description of the Analytical Model

A high-level dynamic opto-electrothermal model was developed in order to accurately simulate and predict the behavior of the detector. This model incorporates the Monte-Carlo ray-trace (MCRT) method to model the optical behavior of the detector, and a finite-element model to characterize the electrothermal behavior of the detector. In addition, an algorithm to correct the detector output for optical cross-talk was developed and integrated into the model. This end-to-end model was implemented in a FORTRAN program titled **Detector.f**. Figure 4.1 provides a logic flowchart for **Detector.f**.

4.1 Optical model

4.1.1 Detector cavity

The thermopile detector is mounted in a wedge-shaped cavity, as shown in Figure 1.2. The reason for mounting the detector in a cavity is to increase the number of rays absorbed on each pixel of the detector, through specular reflections, which leads to enhanced spectral flatness. For this reason, the walls of the cavity are highly reflective and highly specular. The values for the reflectivity and specularity ratio, defined as the ratio of the specular
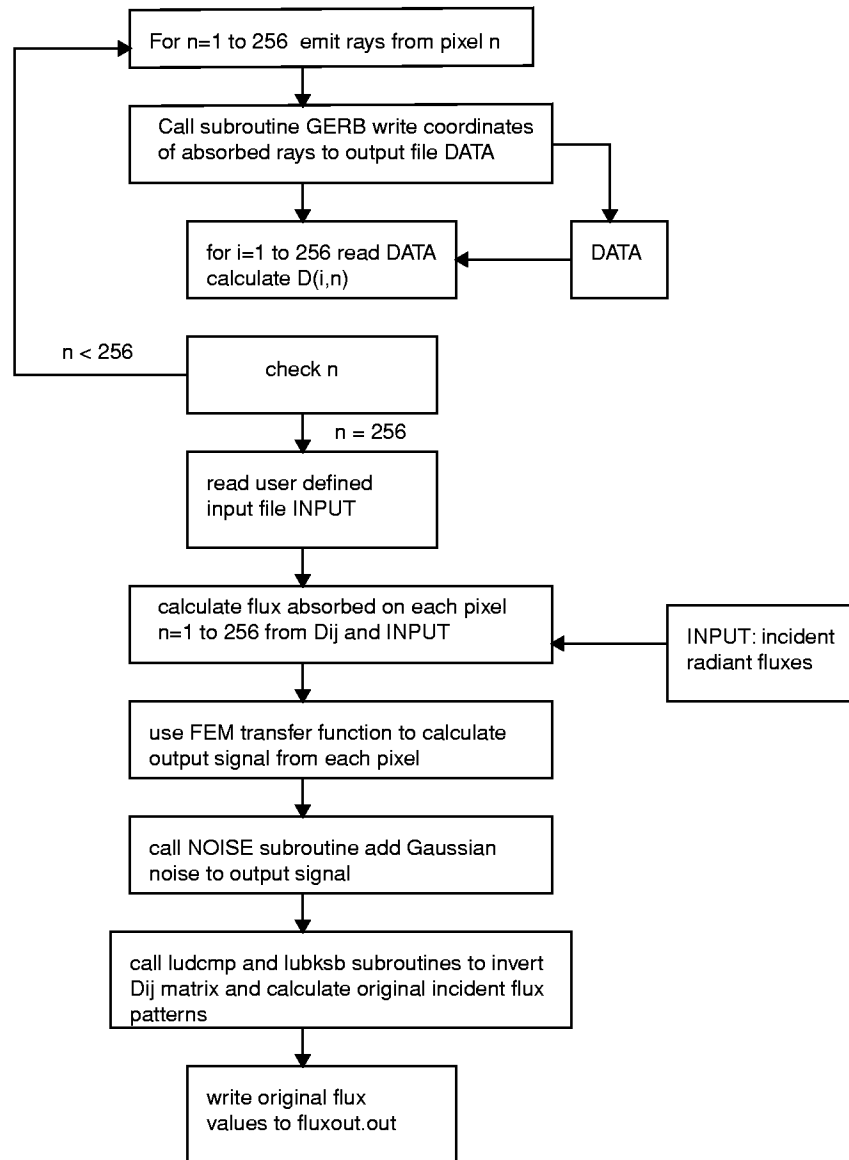
Figure 4.1: Flowchart for **Detector.f**

component of reflectivity over the overall reflectivity, used in the model are both 0.9. The thermopile detector contains an active and a reference junction, with the active junction being visible to incident radiation and the reference junction being shielded. The active junction requires a high absorptivity and a high specularity ratio. To achieve this, the active junction is coated with a black absorber coating such as CHEMGLAZE Z-306. A specularity ratio of the detector of less than unity creates optical cross-talk, as some rays are reflected diffusely and are absorbed by pixels other than the pixel to which they are initially incident. Further discussion of optical cross-talk appears later in the thesis.

Sánchez [1998] performed a study of the optical characteristics of the cavity and determined that a wedge angle of 45 deg provides the most uniform distribution of rays across the surface of the detector and the least optical cross-talk. For these reasons this was the angle used in the current end-to-end model.

4.1.2 Monte-Carlo ray-trace model

The optical behavior of the cavity was modeled using the Monte-Carlo ray-trace (MCRT) method. A FORTRAN program titled **GERB**, developed by Sánchez [1998], was modified and used as a subroutine in **Detector.f**. The program reads an input file that can be modified by the user, and that specifies the radiometric flux initially incident to each of the 256 pixels in the linear array. It then uses the MCRT method to calculate a modified distribution factor (D'_{ij}). The original distribution factor defined (D_{ij}) is defined as the number of rays emitted from surface i that are absorbed by surface j over the total number of rays emitted from surface i, for each pixel [Mahan and Eskin, 1984]. The modified distribution factor (D'_{ij}) is defined as the number of rays incident to surface j that are absorbed by surface i over the total number of rays incident to surface j. These values are then used to calculate the total flux absorbed by each pixel.

4.1.3 Optical cross-talk

As stated above, the diffuse component of reflectivity of the surface of the active junction and the cavity walls causes energy to be absorbed by pixels on the detector array other than the pixel on which it was initially incident. This is termed optical cross-talk. It is possible to eliminate this cross-talk through post-processing and to recover the values of the original incident energy. The post-processing algorithm is based on the "discrete" Green's function.

Mahan et al. [1998] have shown that the energy absorbed, X_i, on pixels $i = 1 \ldots n$ can be represented as the sum of the absorbed portion of the incident energy, X_i^{abs}, and the energy absorbed due to reflections, X_i^{ref},

$$X_i = X_i^{abs} + X_i^{ref} . \tag{4.1}$$

The energy absorbed on initial incidence can be expressed as the product of the absorptivity of pixel i, α_i, and the energy originally incident to i, Φ_i. The energy absorbed due to reflections can be expressed as the product of the discrete Green's function G_{ij} and the radiation initially incident to pixel j, Φ_j, for pixels $j = 1 \ldots n$. The discrete Green's function is defined as the radiation initially incident to surface j that is reflected and ultimately absorbed by surface i. Equation 4.1 can then be rewritten

$$X_i = \alpha_i \Phi_i + G_{ij} \Phi_j . \tag{4.2}$$

Introducing the Kronecker delta function, defined

$$\delta ij = \left\{ \begin{array}{ll} 1 & i = j \\ 0 & i \neq j \end{array} \right. , \tag{4.3}$$

Equation 4.2 can rewritten

$$X_i = (\alpha_i \delta_{ij} + G_{ij}) \Phi_j . \tag{4.4}$$

We can utilize the properties of the MCRT method to deconvolve the output. The distribu-

tion factor D'_{ij} in the current application is estimated

$$D'_{ij} \cong \frac{N_{ij}}{N_j} \, ,$$ (4.5)

where N_j is the number of rays initially incident to surface j and N_{ij} is the number of rays initially incident to surface j that are absorbed by surface i. The matrix D'_{ij} is obtained by illuminating each pixel j separately with a fixed number of rays (typically on the order of 10^6) and recording the number of rays absorbed in each pixel i. The result is a n-by-n matrix of D'_{ij} values, where n is the number of pixels in the linear array, that completely describes the distribution of rays between the aperture and the linear array detector (it should be noted that this matrix does not represent rays absorbed by the cavity walls). Using the D'_{ij} matrix, the relationship between the energy originally incident to the pixels (Φ_j) and the energy absorbed by the pixels (X_i) is simply

$$[X_i] = [D'_{ij}][\Phi_j] \, .$$ (4.6)

We see that Equation 4.6 is in the same form as Equation 4.4 and that D'_{ij} is identical to the quantity $\alpha_i \delta_{ij} + G_{ij}$.

Since the D'_{ij} matrix is only dependent on the surface properties and geometry of the cavity, we can recover the original input to the cavity as long as we can determine the energy absorbed on each pixel. This is accomplished by a simple matrix inversion, that is

$$[\Phi'_j] = [D'_{ij}]^{-1}[X_i] \, ,$$ (4.7)

where Φ'_j is the estimated flux initially incident to pixel j.

The value for the absorbed energy on each pixel, X_i, is related to the pixel output voltage according to

$$V_i = \Re X_i \, ,$$ (4.8)

where $\Re$ is the responsivity of the detector in V/W. Some electrical noise will be added to the signal before the absorbed energy can be determined. This will compromise the accuracy of the recovered data, and is the subject of a study later in the thesis.

4.2 Thermoelectric model

In order to predict the output of the detector, it is necessary to compute the temperature distribution in each pixel, which consists of a thermopile thermal radiation detector. This is achieved by creating a thermoelectric model of the detector using a commercial finite element software package, ALGOR [ALGOR, 1993].

The proposed sensor design is a linear-array thermal radiation thermopile detector. The sensor uses a differential thermopile arrangement to detect incident radiant heat flux (energy per unit time per unit area). The detector is composed of a pattern of thermocouple junction pairs, each containing an active junction and a reference junction, electrically connected in series. Referring to Figure 4.2, the active junction consists of an absorber layer, a layer of zinc-antimonide, a layer of platinum, and a layer of parylene bonded to an aluminum-nitride substrate. The reference junction consists of a layer of zinc-antimonide and a layer of platinum bonded to the same aluminum-nitride substrate. The two junctions are electrically connected by a zinc-antimonide bridge, that connects the zinc-antimonide layer in the two junctions. As heat flux is absorbed by the two junctions, the reference junction is able to dissipate heat directly to the substrate and thus more rapidly than the active junction, due to the insulating layer under the active junction. This causes the temperature of the active junction to rise more rapidly than that of the reference junction, and so a temperature difference is produced. The two junctions produce voltages proportional to their temperatures but with opposing polarities. The net result is a positive voltage, equaling the algebraic sum of the two, that is proportional to the temperature difference and, at steady state, proportional to the radiant heat flux. The output voltage is related to the temperature difference
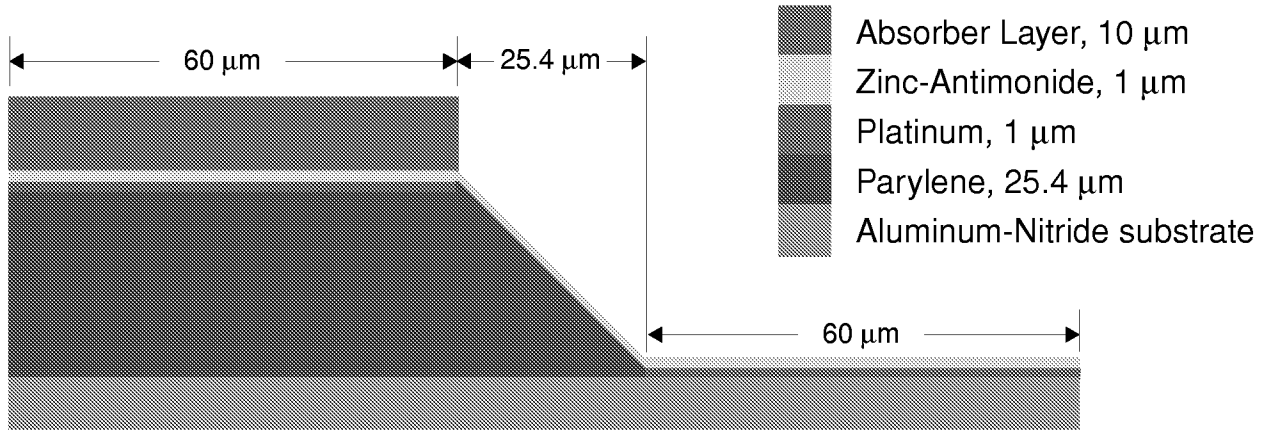
Figure 4.2: Two-dimensional geometry of a single thermocouple pair

between the two junctions by

$$V = S_{AB}\Delta T \, , \tag{4.9}$$

where S_{AB} is the Seebeck coefficient having a nominal value of 920 $\mu V/K$ for the platinum/zinc-antimony combination used in the detector.

The two-dimensional geometry of each pixel, or thermocouple pair, is represented in Figure 4.2. The nominal material properties are given in Table 4.1. For more information on the thermoelectric characteristics of the detector, the reader is referred to Weckmann [1997].

Table 4.1: Nominal material properties

	Mass Density (kg/m^3)	Specific Heat (J/kgK)	Conductivity (W/mK)
Platinum	21450	133	71.6
Zinc Antimony	6880	200	60
Aluminum Nitride	3260	800	165
Parylene	1289	712	0.084
Chemglaze Z-306	1400	669	0.209

4.2.1   General assumptions and approximations

The following assumptions and approximations were made in the thermoelectric model:

- Conduction and radiation are the only modes of heat transfer present in the analysis, as the detector and cavity operate in a vacuum environment.

- Heat transfer via radiation between the detector and cavity walls is considered negligible since the walls and substrate are maintained at a constant temperature of 311 K, which is within a fraction of a millikelvin of the temperature throughout the pixel.

- No significant variation in the material properties with temperature occurs, as the temperature differences and variations are small.

- No electrical current passes through the thermocouple junctions because the signal-conditioning electronics used to monitor the voltage output has an effectively infinite impedance.

- Each thermocouple junction is isolated from the neighboring thermocouple junctions by a 3-μm vacuum gap. A heat flux boundary condition is applied to the active junction, which represents the net absorbed portion of the incident radiation from the scene being viewed. The substrate is maintained at 311 K, and represents a constant temperature boundary condition at the bottom of the thermocouple junction. All other surfaces of the junction pair are insulated, as indicated in Figure 4.3.

4.2.2   Finite element model

A two-dimensional finite element model was created to determine the temperature distribution in the thermocouple junction. A mesh consisting of 4007 nodes was used, with a constant heat flux applied to the absorber layer and with the bottom of the junction maintained at a constant uniform temperature. A 10-μm thick portion of the substrate was included in
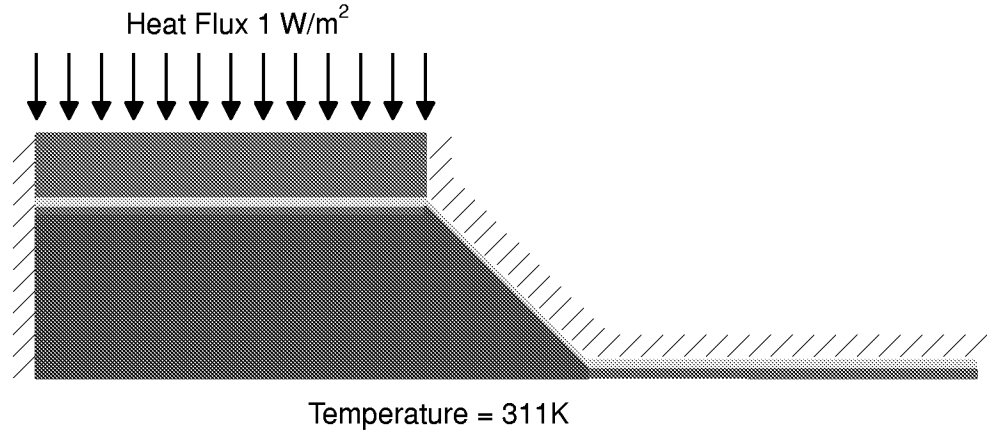
Figure 4.3: Boundary conditions for two-dimensional heat transfer analysis of a thermocouple junction

the model, to test for possible conduction through the substrate between the active and reference junctions. A variable shift $\theta = T - 311$ was applied because of the extremely small temperature gradients in the junction (on the order of 10^{-4} K). The software used, ALGOR, supplies a maximum of four significant figures, so an applied temperature of 311 K would cause the actual temperature variation to be submerged in round-off error. Using the variable shift, the base temperature becomes 0 K and the temperature range in the junction is then on the order of 10^{-4} K.

4.3   Noise analysis

In order to accurately model a real instrument, it is necessary to simulate the Gaussian noise associated with the detector and the electronic components of the instrument. This noise may be thought of as a pertubation to the signal.

To simulate the noise, we begin with the assumption that the noise associated with the signal has a Gaussian, or normal, probability distribution function (*pdf*) given by

$$pdf(x) = \frac{1}{\sigma\sqrt{2\pi}} \exp\left[\frac{-(x-\mu)^2}{2(\sigma)^2}\right]. \tag{4.10}$$

The cumulative distribution function (cdf) is defined as

$$cdf(z) = \int_{-\infty}^{z} pdf(x)\,dx \qquad (4.11)$$

and gives the probability that a normally distributed random variable Z will be less than or equal to z. Because noise has a positive value between 0 and ∞ , the lower bound of the integral can be changed to 0 and Equation 4.11 can be written

$$cdf(z) = \int_{0}^{z} \frac{1}{\sigma\sqrt{2\pi}} \exp\left[\frac{-(x-\mu)^2}{2(\sigma)^2}\right] dx \; . \qquad (4.12)$$

Evaluation of this integral gives

$$cdf(z) = -\frac{1}{2} erf\left[\frac{\sqrt{2}}{2}\frac{(-z+\mu)}{\sigma}\right] + \frac{1}{2} erf\left[\frac{\sqrt{2}\mu}{2\sigma}\right] \; . \qquad (4.13)$$

The error function can be well approximated by

$$erf(x) = \frac{2}{\sqrt{\pi}} \sum_{n=0}^{\infty} (-1)^n \frac{x^{2n+1}}{n!\,(2n+1)} \; . \qquad (4.14)$$

Combining Equations 4.13 and 4.14 gives

$$cdf(z) = -\frac{1}{\sqrt{\pi}} \sum_{n=0}^{\infty} (-1)^n \frac{A^{2n+1}}{n!\,(2n+1)} + \frac{1}{\sqrt{\pi}} \sum_{n=0}^{\infty} (-1)^n \frac{B^{2n+1}}{n!\,(2n+1)} \; , \qquad (4.15)$$

where

$$A = \frac{\sqrt{2}}{2}\frac{(-z+\mu)}{\sigma}$$

and

$$B = \frac{\sqrt{2}\mu}{2\sigma} \; .$$

The cumulative distribution function has a property such that "if X is a random number, and we have the cdf, $F_x(X)$, and if $F_x(X)$ is continuous, the random variable Y produced by

the transformation $Y = F_x(X)$ has a uniform distribution over the interval (0,1)"[Gibbons and Chakraborti, 1992]. This property allows us to generate an equally distributed random number between 0 and 1, assign this value to cdf (x), and solve for x. This generates a normally distributed random variable x from a uniformly distributed random number generator.

This principle was applied to the end-to-end model to add noise to the output signal of the detector. A value for the standard deviation, σ, is specified in the program, and the value for the output signal of the thermocouple junction pair is assigned to the mean, μ. A random number between zero and unity is generated, and Equation 4.15 is used to calculate a new value for the signal, which lies on a normal distribution around the mean, or original signal output. This procedure is repeated for each thermocouple junction pair.

To test the validity of this procedure, a value of unity was assigned to μ and a value of 0.1 was assigned to σ and $n = 10,000$ noise values were calculated using the subroutine **noise2.f**. A histogram of these values is shown in Figure 4.4. The normal distribution curve is well represented by the histogram, with some small error in the wings due to truncating the infinite series expansion of Equation 4.15.
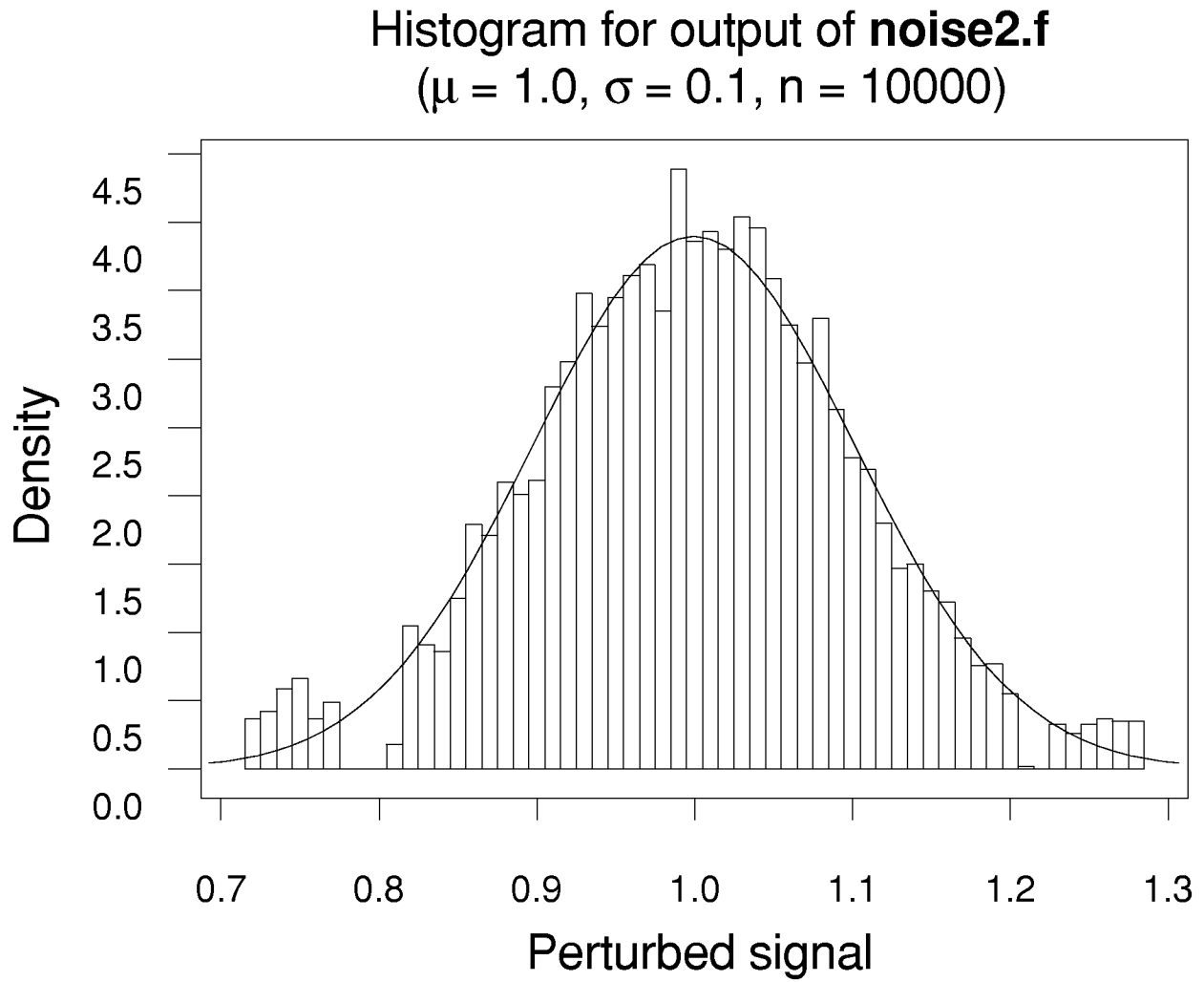
Figure 4.4: Histogram of noise distribution

Chapter 5

Results and Discussion

5.1 Finite element analysis

5.1.1 Thermal cross-talk

One of the assumptions made in formulating the thermoelectric model of the detector is that each of the 256 individual thermocouple junctions (pixels) is thermally isolated from its neighbors by a 3-μm gap that penetrates approximately 10 μm into the aluminum-nitride substrate. To test this assumption, a thermal analysis of two neighboring pixels was performed. It was assumed that radiative exchange between the two pixels was negligible, and the only mode of thermal interaction was conduction through the detector's substrate. Furthermore, it was assumed that all interactions would most likely occur between the active junctions, as the reference junctions are maintained at the temperature of the substrate. A second two-dimensional model was created, this time in the y-z plane of the thermocouple-pair, at $x = 0$, with 100 μm of the substrate included to allow for conduction through it. Symmetry was assumed to justify an insulated boundary condition to the two sides of the model. The bottom of the included portion of the substrate was given a uniform temperature boundary condition of 0 K. One pixel was given a flux boundary condition of 1 W/m^2 while
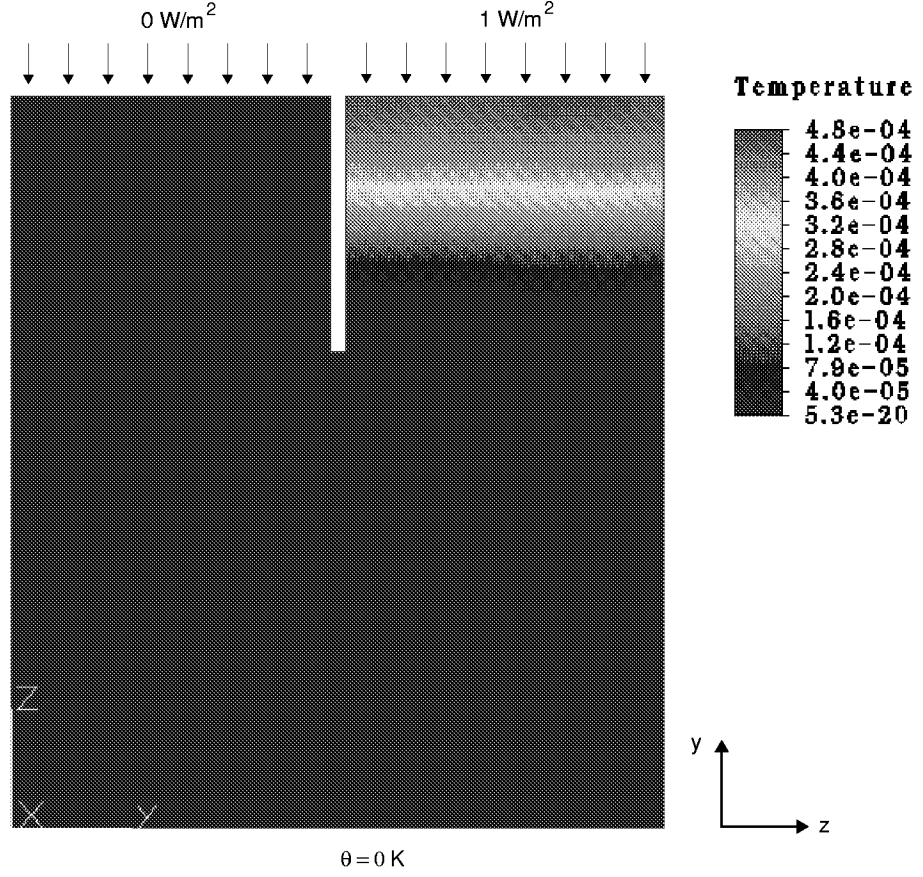
Figure 5.1: Two-dimensional temperature distribution of two neighboring active thermocouple junctions in the y-z plane at $x = 0$

the other was allowed to thermally interact with the cavity at $\theta = T_\infty - 313K = 0K$ through thermal radiation. The steady-state temperature distribution of the two pixels is shown in Figure 5.1. From the figure it is clear that conductive heat transfer between the pixels is negligible. This is most likely due to the thermal impedance layer under each pixel, which acts not only to create a temperature difference between the active and reference junctions of each thermocouple-pair, but also to isolate them from their neighbors.

5.1.2 Two-dimensional model

In order to determine the output of the detector, it is necessary to accurately determine the temperature distribution in the active and reference junctions of the thermocouple junction pair. The question arises of which temperature to use in Equation 4.9, however, as the temperature is not uniform throughout the active junction. Weckmann [1997] argues convincingly that the output of the thermocouple junction should be dependent only on the highest temperature in the active junction due to the law of intermediate temperatures, and that the difference between this highest temperature and that of the reference junction should be used with the Seebeck coefficient to determine the output. This is the approach used here.

In order to determine where in the active junction the highest temperature occurs, the two-dimensional finite element model of the thermocouple junction was used under steady-state conditions with the active junction illuminated with a heat flux of 1 W/m^2. The resulting steady-state temperature distribution for the thermocouple junction is shown in Figure 5.2.

It was found from the temperature distribution that the temperature in the active junction does not vary in the y-direction, but does vary somewhat in the x-direction. Figure 5.3 shows the temperature in the active junction from $x = 1$ to $x = 60$ μm. The highest temperature in the active junction with uniform heating is at $x = 0$ μm, and the temperature at this point is used in all subsequent cases of uniform illumination to determine the voltage output of the thermocouple junction.

Another property of the thermocouple junction that is of interest is the spatial sensitivity of the detector to a "limited" source. In other words, the active junction is illuminated by a limited source at different locations to determine if the detector response is sensitive to position. The two-dimensional finite element model was once again utilized to study this question. Due to the symmetry in the geometry of the detector, there should be no variation in the response of the detector with distance from gap to gap (z-direction), and so only variations in the distance from edge to edge parallel with the gap between the active and
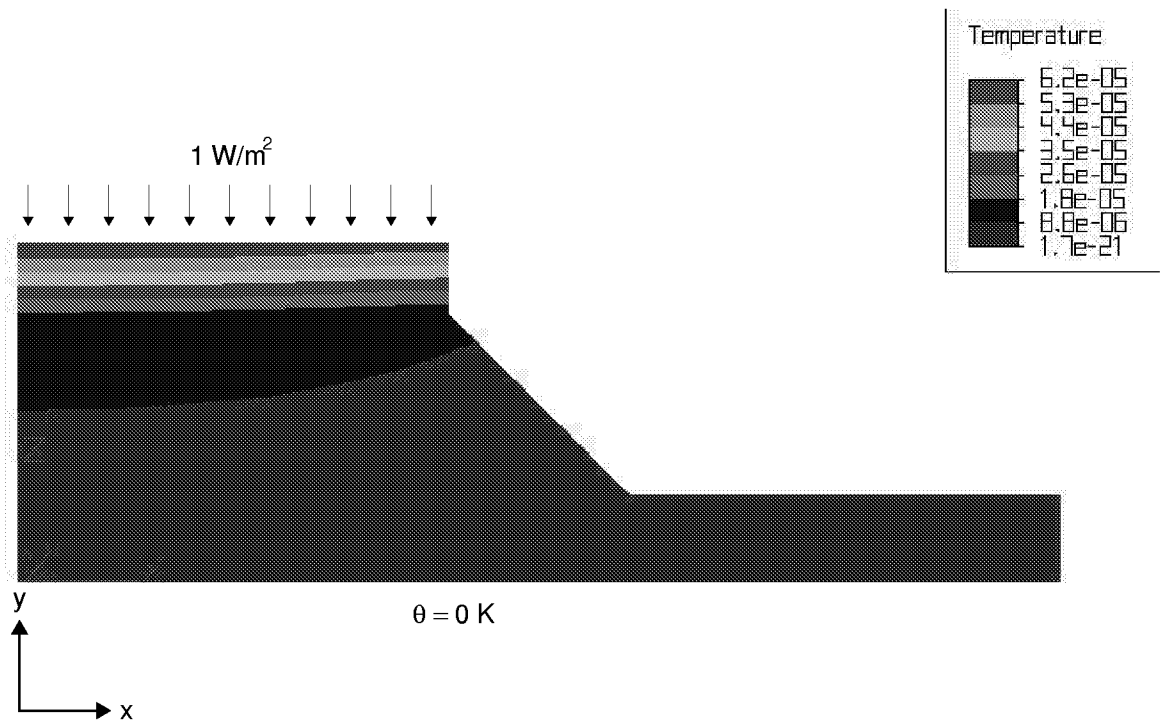
Figure 5.2: Two-dimensional steady-state temperature distribution for a thermocouple junction with the active junction illuminated by a heat flux of 1 W/m^2
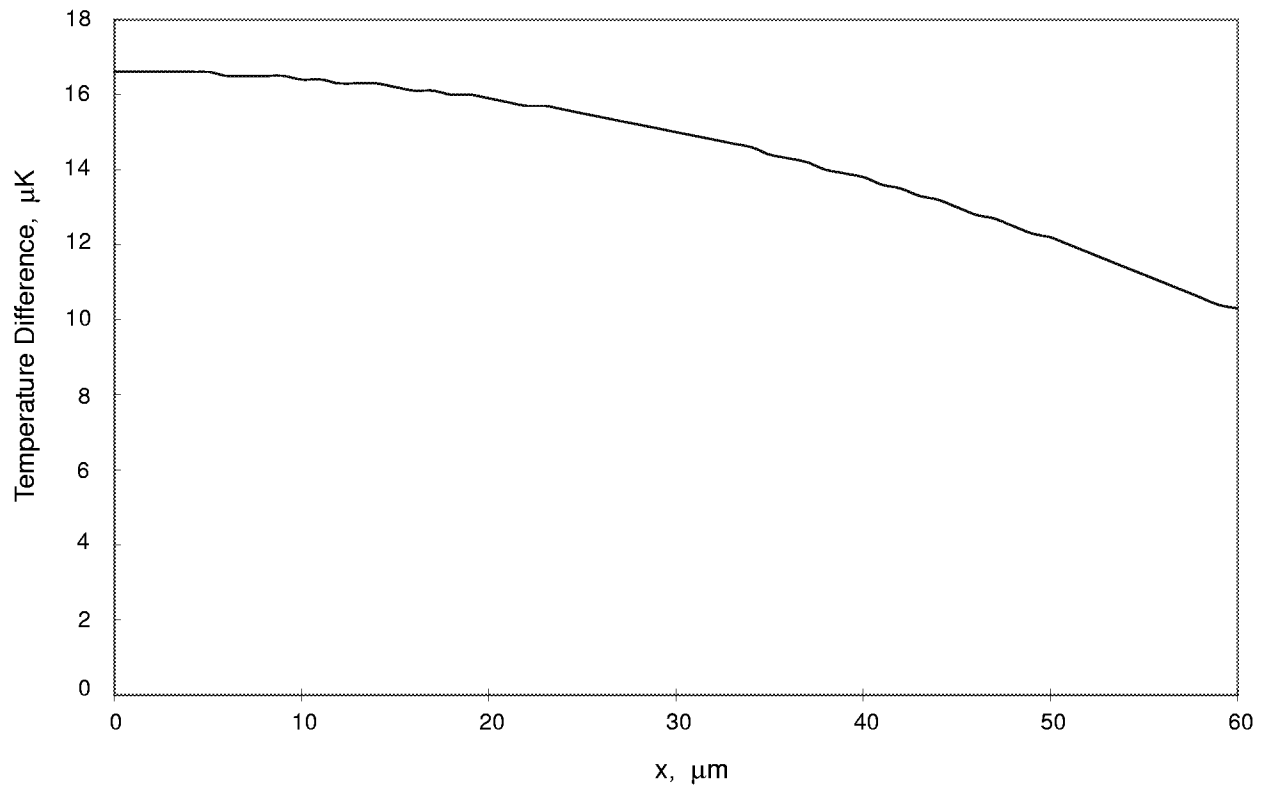
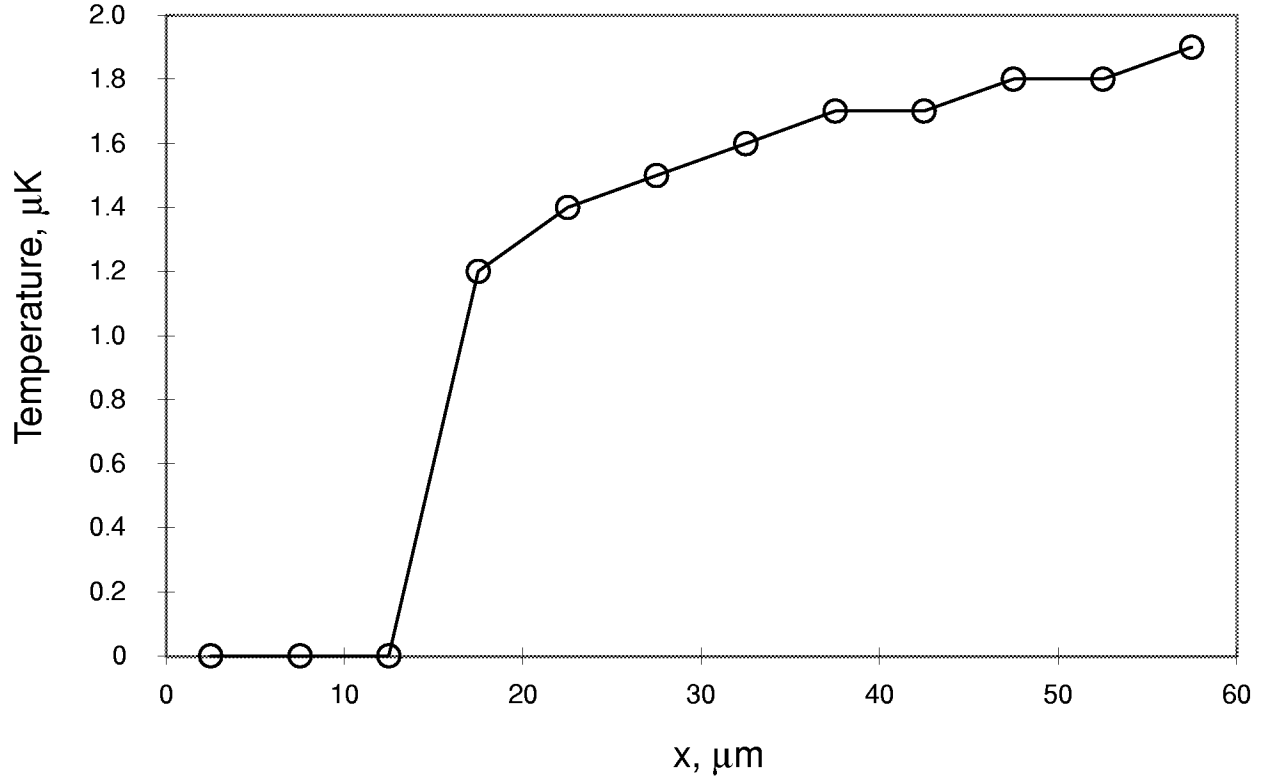Figure 5.3: Active junction maximum temperature as a function of horizontal distance from edge

Figure 5.4: Highest temperature of active junction at it is illuminated at location x by a 5-μm wide 1-W/m^2 source

reference junctions (x-direction) were considered. A 5-μm wide heat flux source of 1-W/m^2 strength was applied at 12 locations, each 5 μm apart, across the 60-μm wide active junction. The resulting highest temperature in the active junction for each of the 12 cases is plotted in Figure 5.4. The highest temperature in the active junction appears to increase when the active junction is illuminated at a position closer to the bridge that separates the active and reference junctions. A much stronger effect but having the same trend was observed experimentally using laser heating [Kist, 1998]. This behavior could be used to aid in future designs of the thermopile geometry.

5.1.3 Determination of the thermocouple junction transfer function

The two-dimensional finite element model permits calculation of the temperature distribution in the thermocouple junction and the associated voltage output. However, due to the nature of the finite element package used, this is not a practical means of determining the output of the thermocouple junction within the larger program, **Detector.f**. Therefore, a transfer function for the thermocouple that could be inserted into **Detector.f** is needed. At this stage, for simplicity, only the zero-frequency transfer function of the thermocouple junction was considered. With this simplification, the transfer function is a function of the absorbed flux alone and can be determined without significant difficulty.

The two-dimensional finite element model was run for ten cases, for absorbed flux values $X = 0.5, 0.6, \ldots, 1.5 \, W/m^2$. The resulting highest temperature difference between the active and reference junctions is shown as a function of absorbed flux in Figure 5.5. The resulting plot is linear, and applying a linear fit over the values results in the desired zero-frequency transfer function, given by

$$\Delta T = 9 \times 10^{-12} + 10^{-5} \, X \, . \tag{5.1}$$

5.2 Optical cross-talk

The proposed detector design makes use of the optical cavity to increase the relative absorptivity of the linear-array of thermocouple pairs. One unfortunate side-effect of the cavity, however, is that a small fraction of the incident radiation is reflected and absorbed by pixels other than those of initial incidence. This can lead to a small error in the output of each pixel.

To determine what effect optical cross-talk has on the instrument, the end-to-end model, **Detector.f**, was used. An input flux of 1 W/m^2 was specified on pixels 101 through 156,
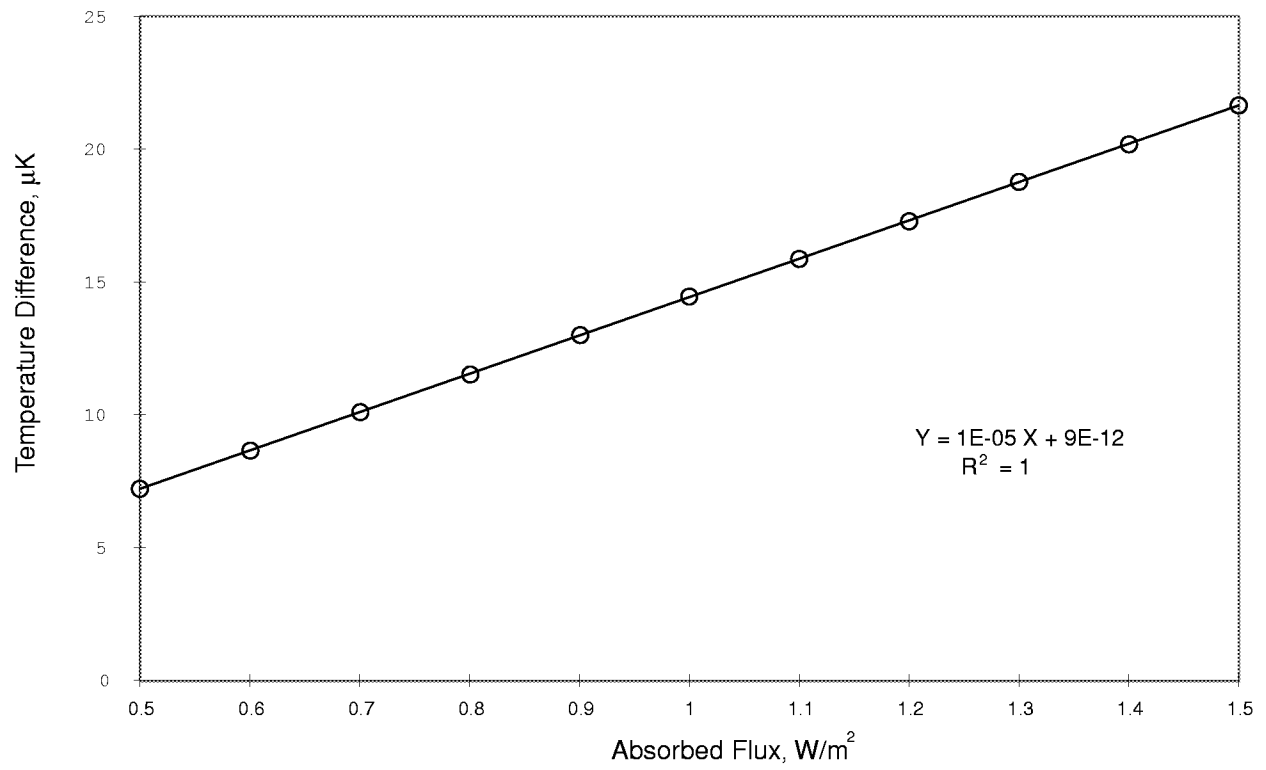
Figure 5.5: Temperature difference between the active and reference junctions of a thermocouple junction as a function of absorbed flux

with the remaining pixels not being illuminated. The output of each pixel was recorded and converted to a flux value, using Equation 5.1. The optical cross-talk on each of these pixels was calculated by subtracting the amount of energy initially incident to each pixel (in this case, $0.9 \ W/m^2$, corresponding to an absorptivity of 0.9 for the illuminated pixels). The optical cross-talk, prior to data post-processing, is shown in Figure 5.6. The greatest fraction of the reflected energy remains in pixels 101, ... ,156, contributing to the enhanced relative absorptivity. However, some spread of energy occurs to pixels not originally illuminated, as can be seen in the rounding of the edges of the original "square" input, and in the small wings that have developed outside the original illuminated region.

The discrete Green's function was utilized to recover the original input energy distribution. Recall from Equation 4.7 that the original energy incident to each pixel can be recovered by inverting the discrete Green's function matrix and multiplying it by the output for each pixel. This method was employed to restore the scattered radiation to the pixel upon which it was initially incident. Figure 5.6 shows the distribution of scattered radiation over pixels $i = 1, \ldots, 256$. The recovered energy distribution over pixels $i = 1, \ldots, 256$ is shown in Figure 5.7. The scattered energy has been put back into the originally illuminated pixels and the original shape of the incident distribution across the array has been recovered. **An important result from Figure 5.7 is that the algorithm has corrected the output for the radiation absorbed by the cavity walls and lost out the aperture!** The maximum value of X_i in Figure 5.6 is slightly higher than 0.05, which indicates approximately 4 to 5 percent of the radiation has been lost to the walls or the aperture. However, the value of $\Phi j'$ in Figure 5.7 for the illuminated pixels is 0.1, which indicates that all the radiant energy has been recovered.
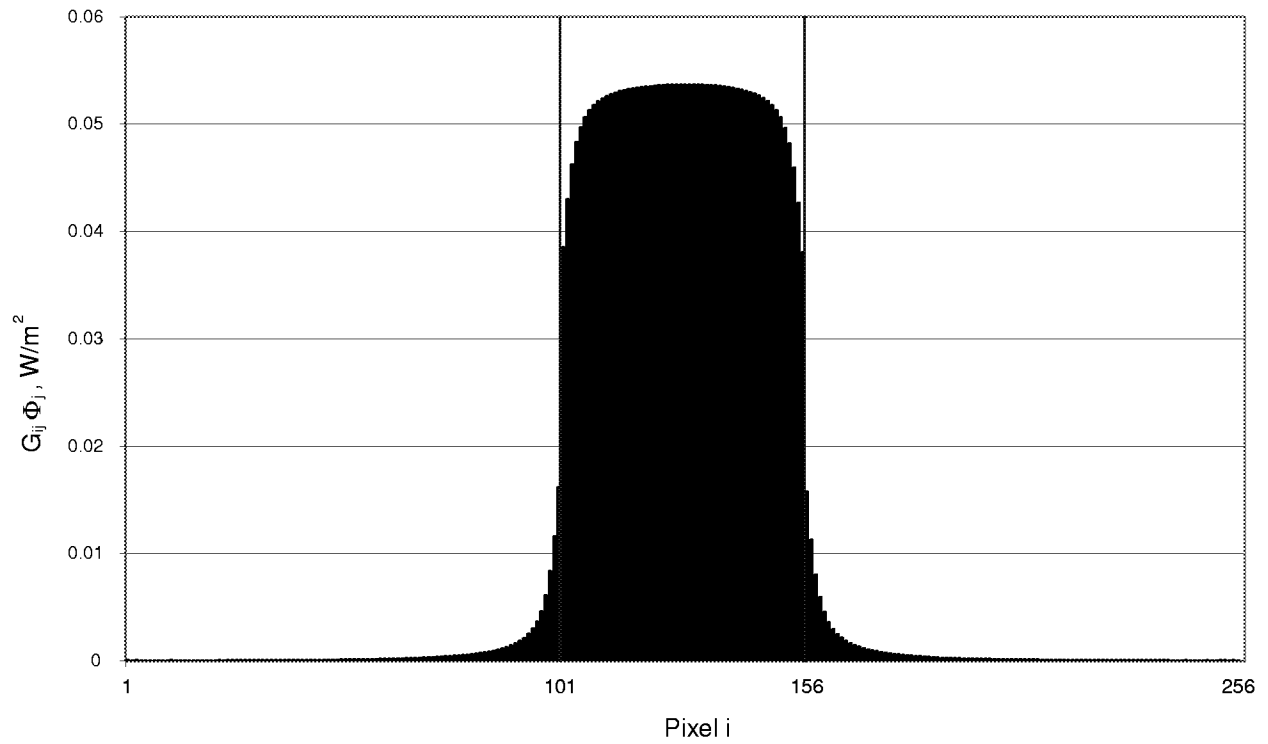
Figure 5.6: Optical cross-talk on the linear-array detector illuminated with a uniform input to pixels 101 through 156, prior to data post-processing
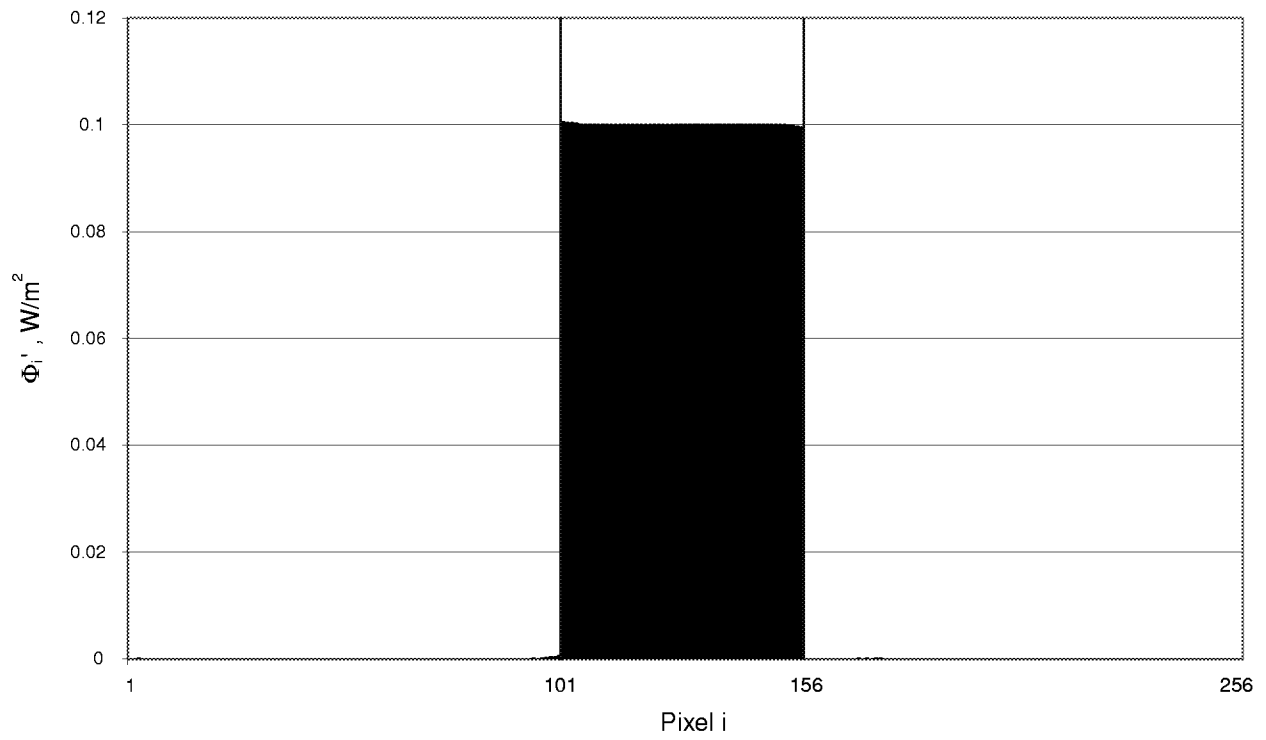
Figure 5.7: Recovered incident flux on the linear-array detector illuminated with a uniform input to pixels 101 through 156, after data post-processing

5.3   Study of detector noise

5.3.1   Effect of data deconvolution on signal-to-noise ratio

It has been shown that the original incident energy can be recovered almost perfectly from the absorbed energy distribution once the discrete Green's function is known. A real instrument, however, would have to recover the original data from a signal with some amount of noise added by the detector and associated electronics. One concern is how the inversion technique using the discrete Green's function, which is essentially a differentiation process, amplifies the noise level of the signal.

To investigate the possible effect of the use of the discrete Green's function inversion technique on a signal with Gaussian noise, the program **Detector.f** was modified to add a noise component with a Gaussian distribution to the output signal. The program was run for three different cases, each representing a different signal-to-noise ratio. The results of these three cases are given in Table 5.1.

For the values in Table 5.1, the mean signal was calculated by taking the mean of the signal values $\langle Y \rangle$ for pixels $i = 101, \dots, 156$ and noise was calculated by considering the variance $\langle Y^2 \rangle$ of the values over this interval. The same method was applied to the recovered flux Φ'_j.

For all three cases presented, the signal-to-noise ratio decreases slightly after the inversion technique is applied. The decrease is approximately 1 percent for all three cases.

Figure 5.8 is a plot of the output signal of the detector with Gaussian noise added, before the discrete Green's function inversion is applied, for the case of a signal-to-noise ratio of approximately 10. Figure 5.9 is a plot of the same signal after the inversion technique is applied.
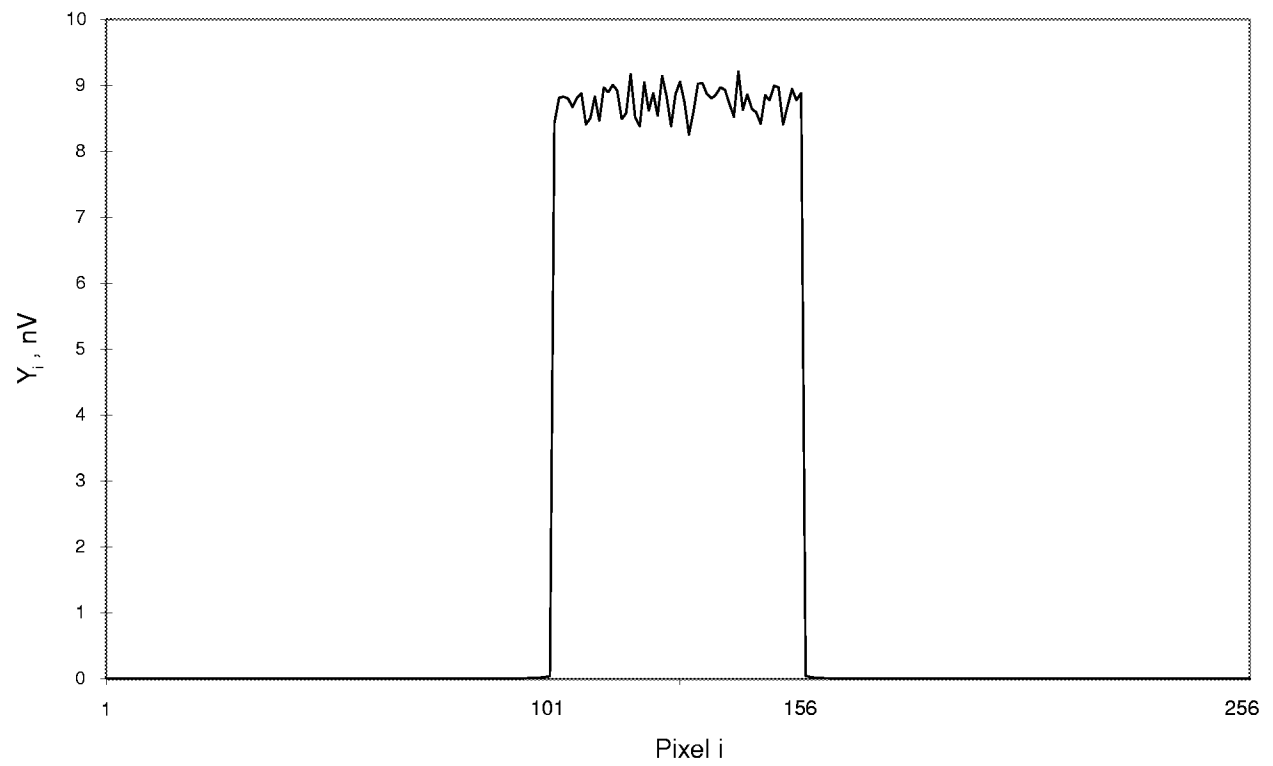
Figure 5.8: Thermocouple junction output signal with Gaussian noise added, signal-to-noise ratio of 10
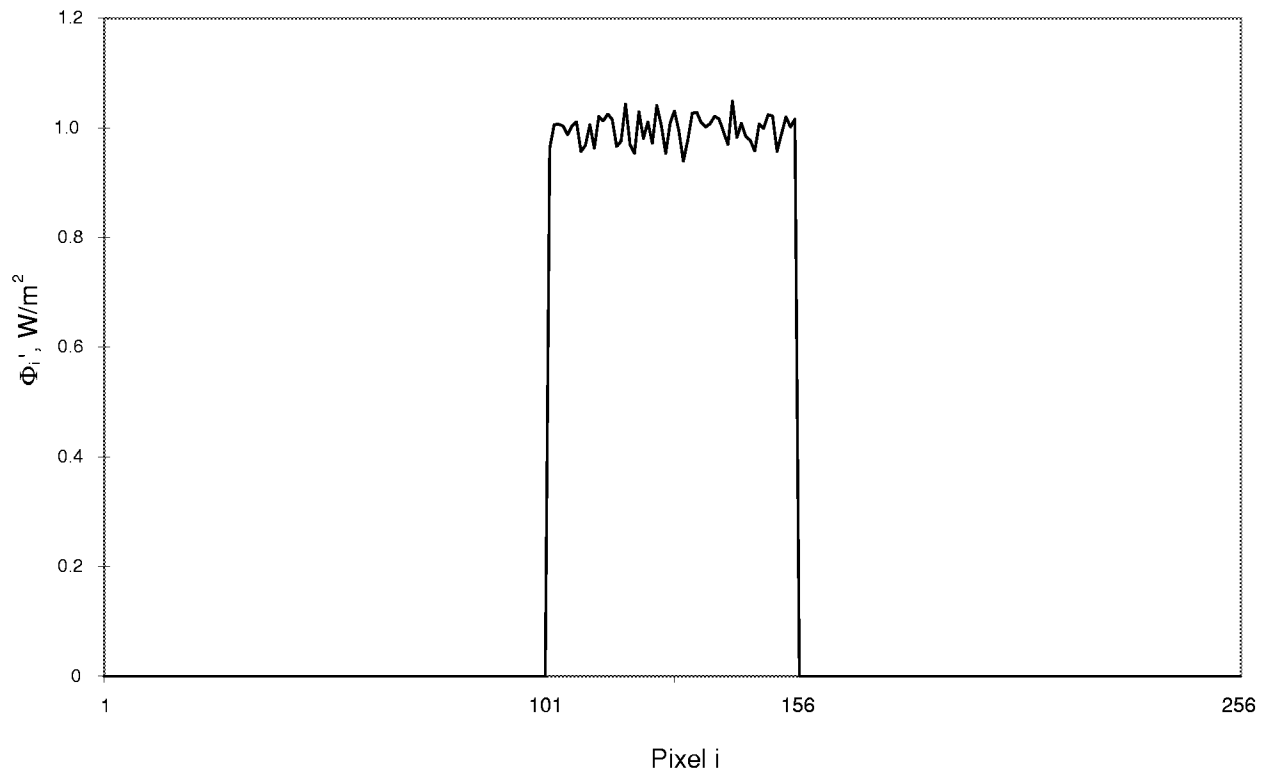
Figure 5.9: Thermocouple junction output signal with Gaussian noise added, signal-to-noise ratio of 10, after data post-processing

Table 5.1: Signal and noise information for output signal of the thermocouple detector prior to and following data processing to recover original signal

	Mean Signal	Noise	Signal-to-noise	% difference
Case 1 output signal Y, nV	8.7454	3.8211	2.289	
recovered flux Φ'_j, W/m^2	0.99572	0.43934	2.266	+0.9749
Case 2 output signal Y, nV	8.7442	1.9097	4.579	
recovered flux Φ'_j, W/m^2	0.99558	0.21959	4.534	+0.9832
Case 3 output signal Y, nV	8.7611	.95405	9.183	
recovered flux Φ'_j, W/m^2	0.99750	0.02618	9.091	+0.9990

$$\% \, difference \equiv \frac{SNR_Y - SNR_{\Phi'_j}}{\langle SNR \rangle}$$

5.4 Parametric study based on the discrete Green's function

As stated in Chapter 4, the discrete Green's function, G_{ij}, is the fraction of radiant energy initially incident to pixel j that is ultimately absorbed by pixel i. This is of interest since it provides a means to measure the scattering in a cavity with the MCRT method. Previously only the total absorbed flux was quantified with this method, through use of the modified distribution factor. Although the discrete Green's function is closely related to the modified distribution factor, there is a subtle difference, and it is of some value to separate the two.

Of some interest is the relationship between the discrete Green's function for a particular cavity and the physical parameters that govern the scattering in that cavity. In the MCRT environment, scattering is quantified by two parameters: the absorptivity, α, defined as the

fraction of energy incident to a surface that is absorbed; and by the specularity ratio, r_s, defined as the fraction of energy reflected from a surface that is reflected specularly. It would be of some value to study the effect of these parameters on the discrete Green's function, with the goal of determining a function to relate them. This would provide a method to determine the distribution of energy in a cavity for any radiant input if the physical parameters are known.

A parametric study was performed to study the sensitivity of the discrete Green's functions to variations in the absorptivity and specularity ratio of the detector surface. The wedge-shaped cavity used in the end-to-end detector model considered elsewhere in this thesis was used in this study also. The program **Detector.f** was modified such that only one pixel, $j = 128$, was illuminated, and the absorbed energy on each pixel $i = 1, \ldots, 256$ was recorded and written to a data file. The program was run for twenty-five cases, corresponding to absorptivity values $\alpha = 0.5, 0.6, \ldots, 0.9$ and specularity ratios $r_s = 0.5, 0.6, \ldots, 0.9$.

The discrete Green's function, $G_{i,128}$, for $\alpha = 0.5$ and specularity ratios $r_s = 0.5, \ldots, 0.9$ is shown in Figure 5.10. Only the Green's functions for $i = 100, \ldots, 156$ were plotted, as all values outside this range were essentially zero. In the plot, it is somewhat difficult to ascertain the variation of $G_{i,128}$ over i as the values at $i = 128$ tend to dwarf the values of the neighboring pixels. To remedy this, Figure 5.11 presents the same results, but with the vertical scale adjusted to display the values of the pixels neighboring pixel $i = 128$. The same vertical and horizontal scale is used for Figure 5.12 through Figure 5.15, which provide plots of $G_{i,128}$ for $\alpha = 0.6, \ldots, 0.9$ and the same range of specularity ratios as in Figure 5.10.

Analysis of Figure 5.11 through 5.15 yields two important facts. First, the values of $G_{i,128}$ decrease as the specularity ratio and the absorptivity increase, and the distribution on i becomes more tightly centered around $i = 128$. This is of course due to there being less energy scattered as the absorptivity increases and less being scattered diffusely as the specularity ratio increases. More interestingly, the shape of the distribution over i remains similar and seems to be scaled with the specularity ratio values, at least over the range of absorptivity

values tested. This suggests that there may exist a relatively simple function that relates these parameters that could be obtained from a multi-variable regression. Surface plots of $G_{127,128}$ and $G_{120,128}$ for $\alpha = 0.5, \ldots, 0.9$ and $r_s = 0.5, \ldots, 0.9$ are given in Figures 5.16 and 5.17, respectively, to illustrate the relationship between the discrete Green's function, absorptivity, and specularity ratio for two individual pixels. The discrete Green's function is shown to be decreasing as both the specularity ratio and the absorptivity increase. This is true for both pixel $i = 127$ (Figure 5.16) and pixel $i = 120$ (Figure 5.17), with the maximum value for the discrete Green's function being smaller for $i = 120$, since the pixel is further from the source of the impulse. Due to the symmetrical nature of the scattered radiation distribution, it is assumed that pixels $i = 129, \ldots, 256$ would have discrete Green's functions similar to pixels $i = 1, \ldots, 127$

Of particular interest is the discrete Green's function where $i = j$, that is the percentage of reflected energy initially incident to a pixel that is absorbed by that same pixel. This represents the true cavity effect, which is an increase in apparent absorptivity of a given pixel due to specular reflections. A surface plot of $G_{128,128}$ for $\alpha = 0.5, \ldots, 0.9$ and $r_s = 0.5, \ldots, 0.9$ is shown in Figure 5.18. It is interesting to note that, unlike the discrete Green's functions for $i \neq j$, which decrease as both the absorptivity and specularity ratio increase, the Green's function for $i = j$ decreases as absorptivity increases but also increases with the specularity ratio, which is opposite the cases where $i \neq j$. This can be explained from the fact that, as the specularity ratio increases, less radiation is reflected diffusely, causing more of the reflected radiation to be absorbed by the pixel to which it was initially incident, and less to be absorbed by the neighboring pixels.

A logical extension of this parametric study is the development of a function that relates the discrete Green's function to the absorptivity and specularity ratio of the detector surface for all the pixels in the linear-array detector. This can be done in the MCRT environment by illuminating individual pixels and recording the distribution factors as defined in this thesis for each pixel, over a range of values for the specularity ratio and absorptivity. A multi-variable regression could then be performed to determine G_{ij} for $i = 1, \ldots, 256$ and
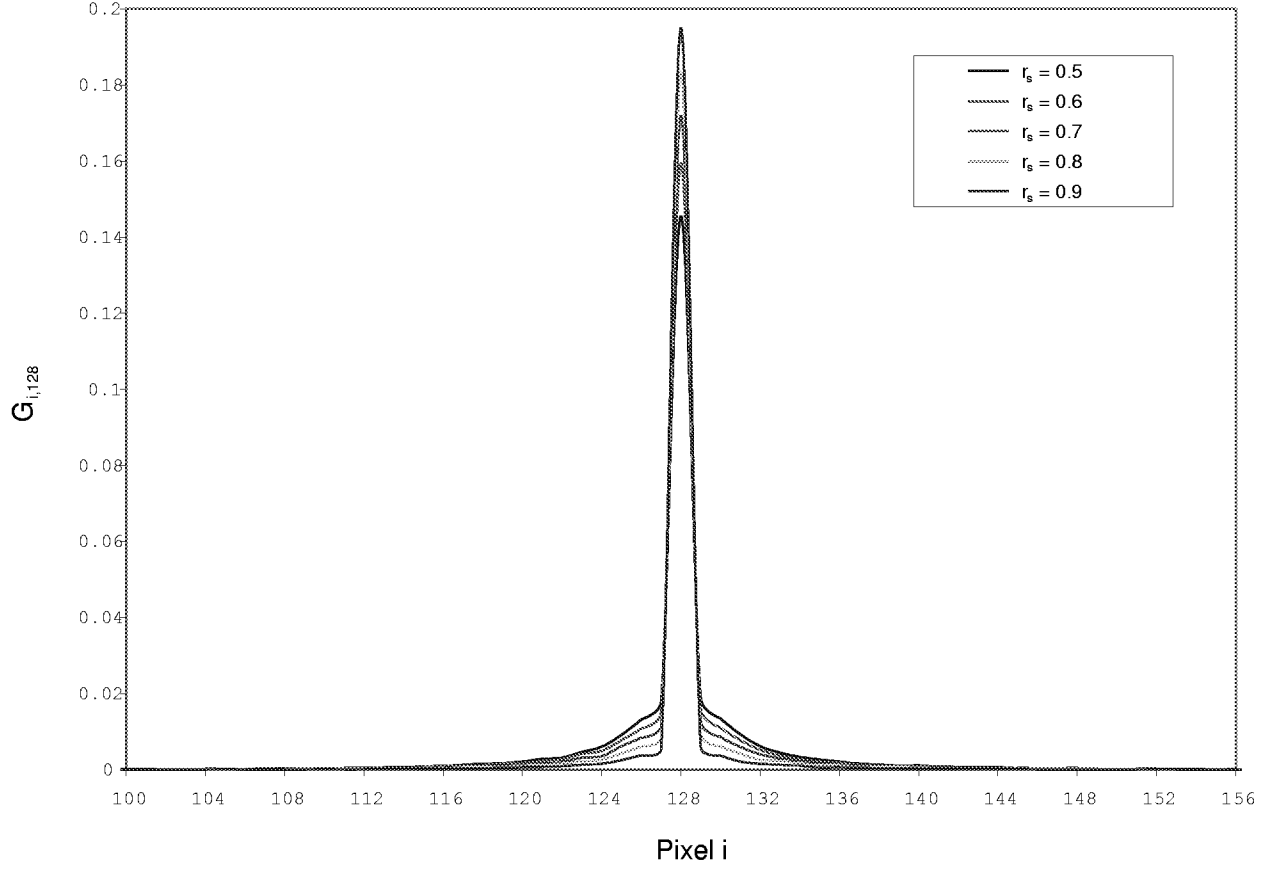
Figure 5.10: Discrete Green's functions, $G_{i,128}$, for $\alpha = 0.5$, $r_s = 0.5, \ldots, 0.9$

$j = 1, \ldots, 256$. Once a relational function is determined, it could be used to characterize the absorptivity and specularity ratio of an unknown detector surface. By actually illuminating an individual pixel, using a laser beam, and measuring the absorbed energy in each pixel, the discrete Green's function for each pixel could be estimated, and the surface properties backed out of the functional relationship.
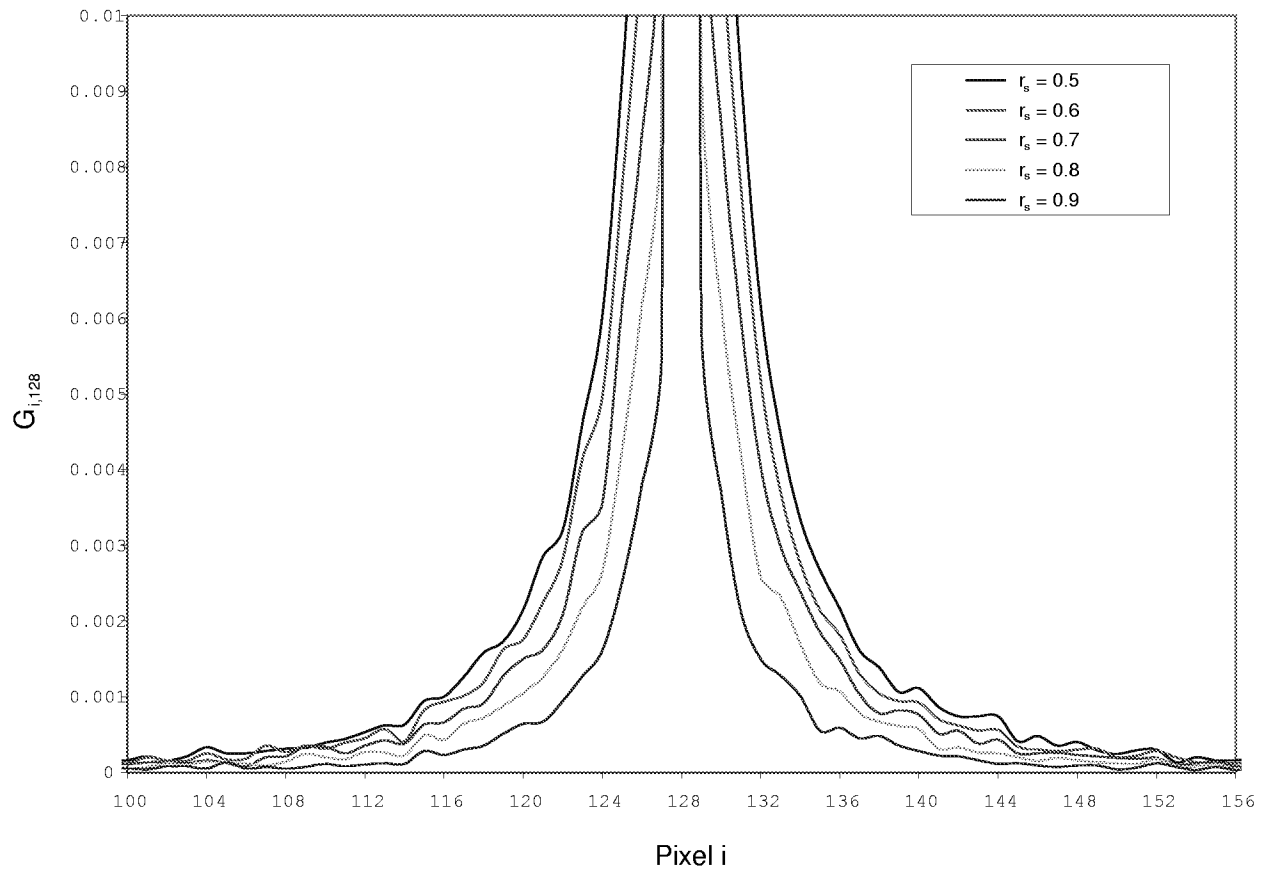
Figure 5.11: Discrete Green's functions, $G_{i,128}$, for $\alpha = 0.5$, $r_s = 0.5, \ldots , 0.9$, with adjusted vertical axis
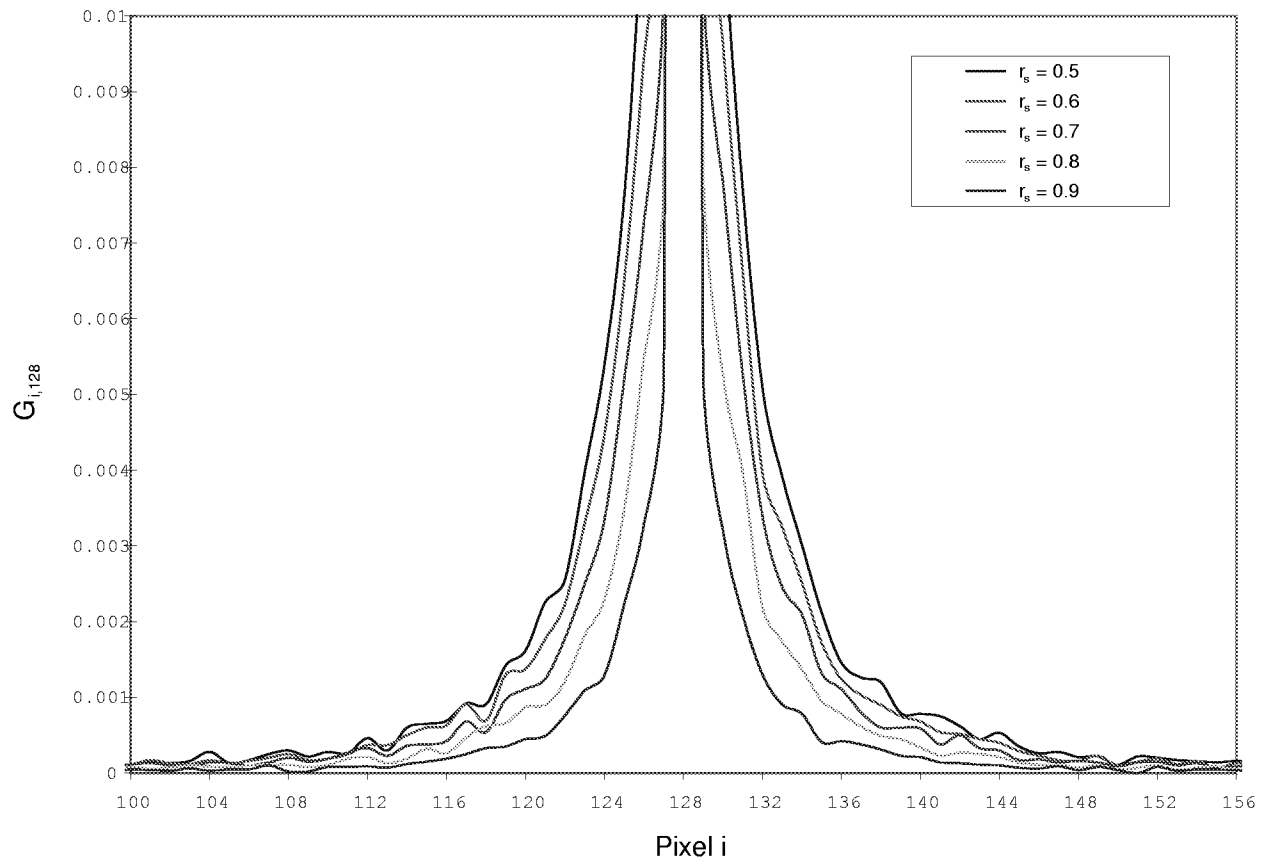
Figure 5.12: Discrete Green's functions, $G_{i,128}$, for $\alpha = 0.6$, $r_s = 0.5, \ldots, 0.9$, with adjusted vertical axis
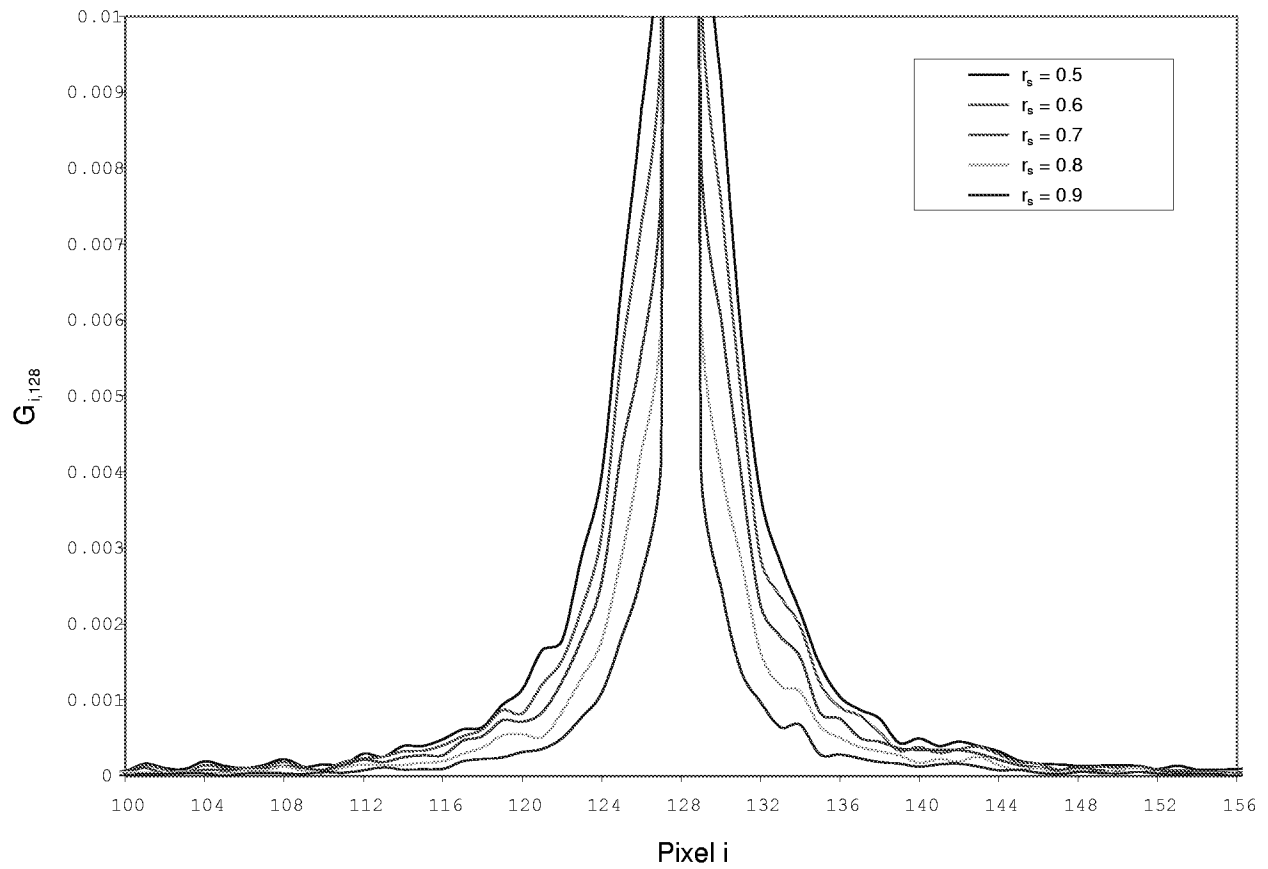
Figure 5.13: Discrete Green's functions, $G_{i,128}$, for $\alpha = 0.7$, $r_s = 0.5, \ldots, 0.9$, with adjusted vertical axis
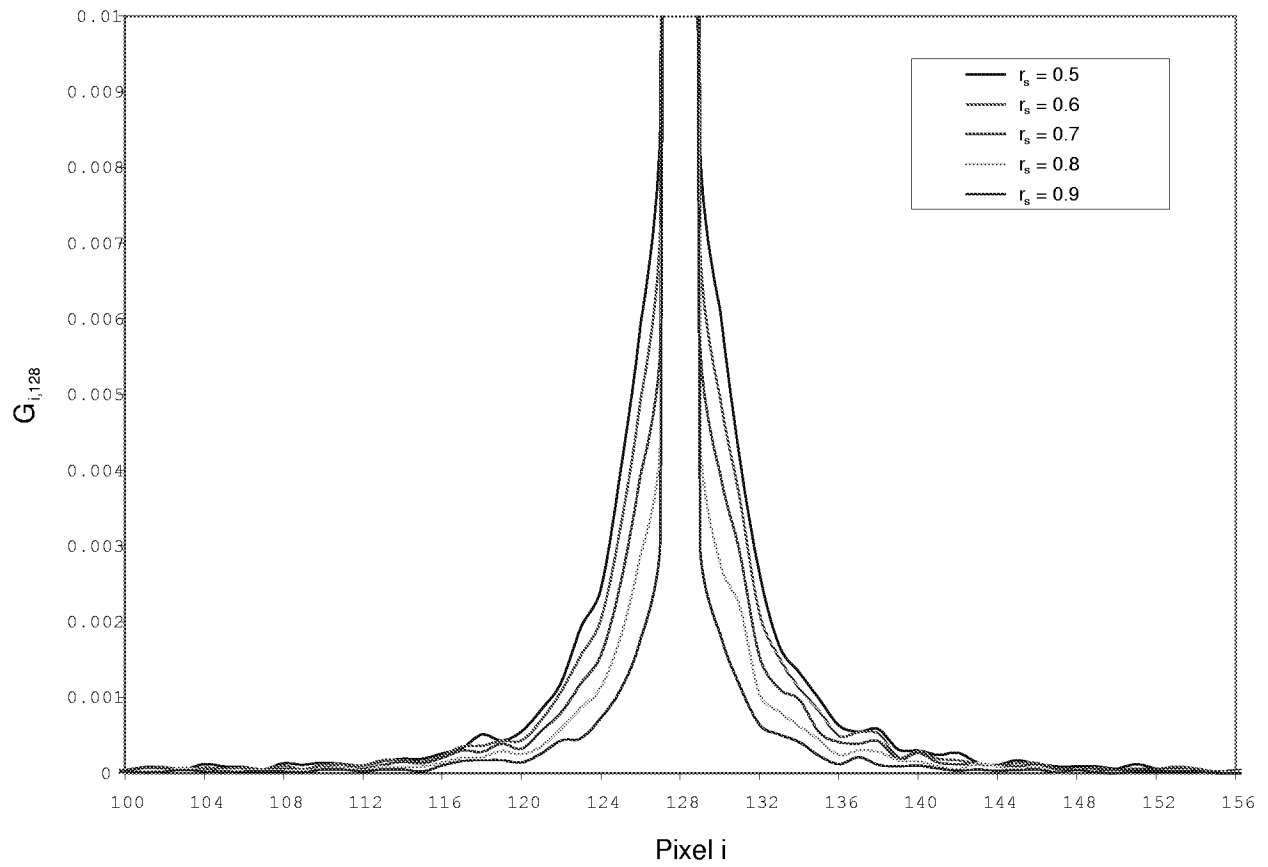
Figure 5.14: Discrete Green's functions, $G_{i,128}$, for $\alpha = 0.8$, $r_s = 0.5, \ldots, 0.9$, with adjusted vertical axis
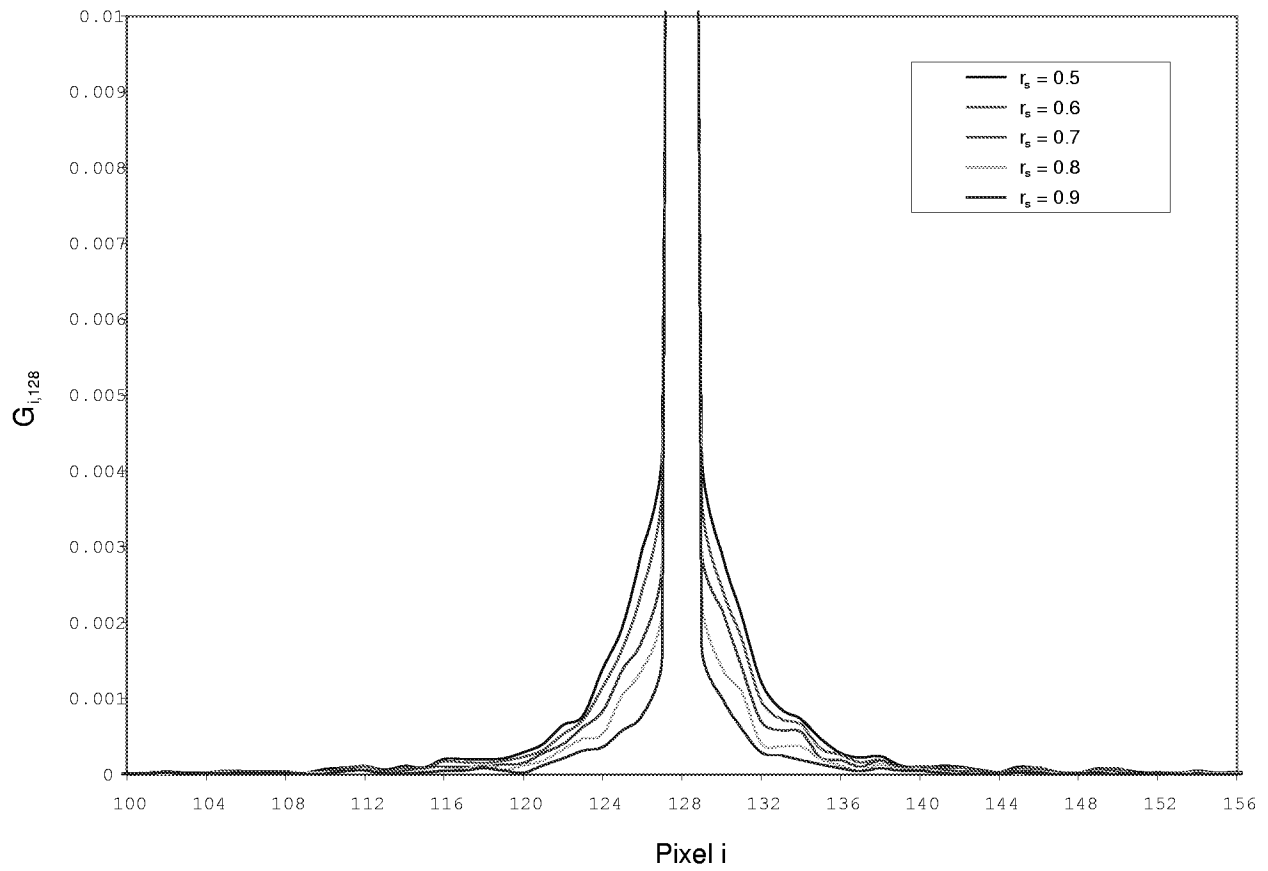
Figure 5.15: Discrete Green's functions, $G_{i,128}$, for $\alpha = 0.9$, $r_s = 0.5, \ldots, 0.9$, with adjusted vertical axis
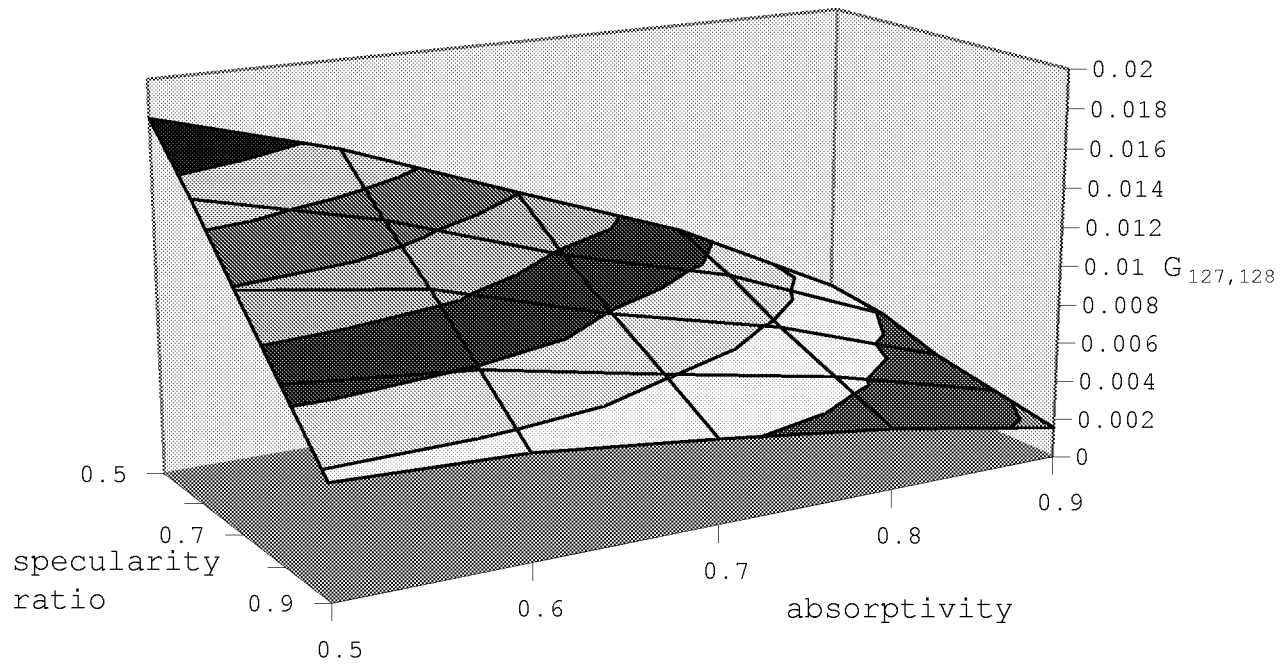
Figure 5.16: Surface plot of the discrete Green's function, $G_{127,128}$, of pixel $i = 127$ for an impulse on pixel $j = 128$, for absorptivity and specularity ratios $0.5, \ldots, 0.9$

Figure 5.17: Surface plot of the discrete Green's function, $G_{120,128}$, of pixel $i = 120$ for an impulse on pixel $j = 128$, for absorptivity and specularity ratios $0.5, \ldots, 0.9$

Figure 5.18: Surface plot of the discrete Green's function, $G_{128,128}$, of pixel $i = 128$ for an impulse on pixel $j = 128$, for absorptivity and specularity ratios $0.5, \ldots, 0.9$
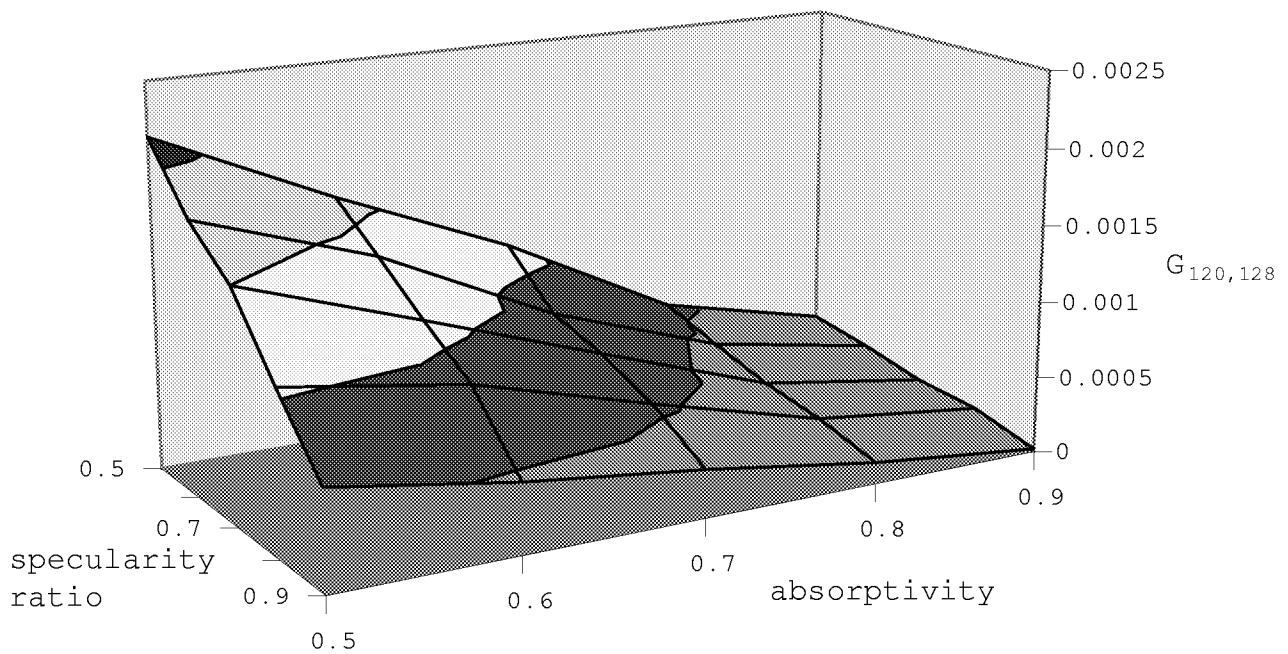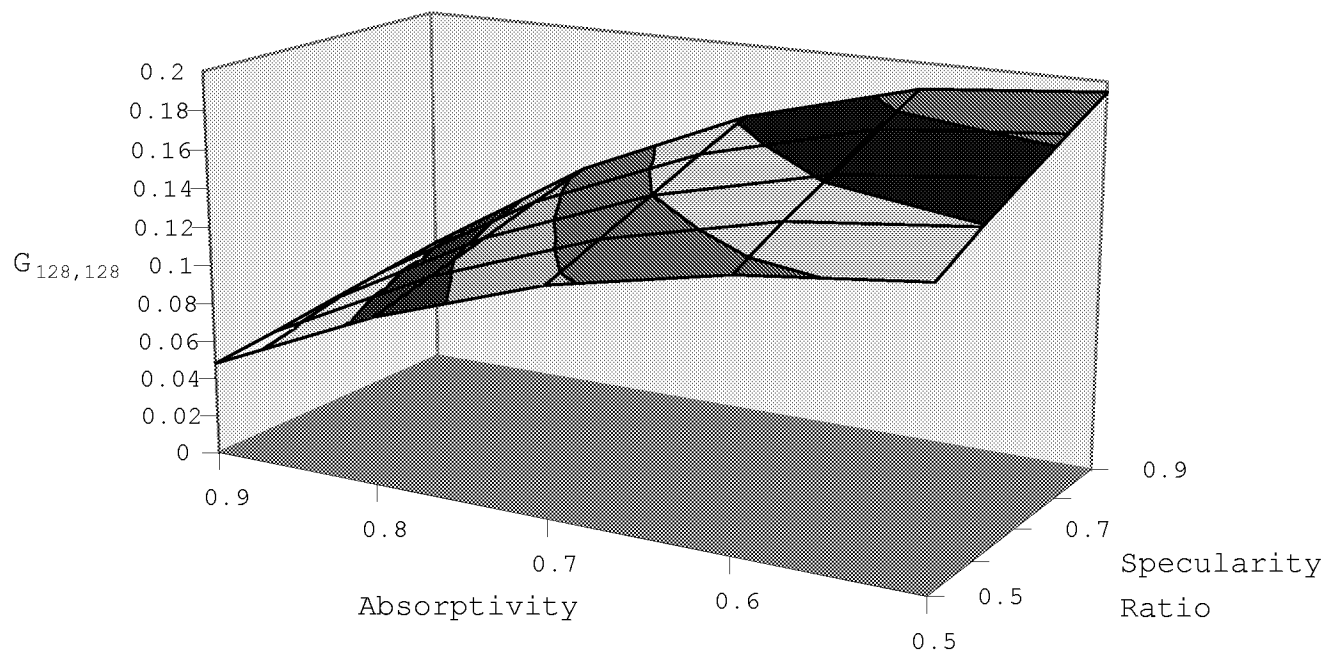
Chapter 6

Conclusions and Recommendations

6.0.1 Conclusions

The following conclusions can be drawn from the research presented in this thesis:

- the two prototype detectors that were tested in the course of this effort had sensitivity values of 883 and 826 $\mu V/W/cm^2$, respectively

- the end-to-end model of the instrument predicted a sensitivity of 870 $\mu V/W/cm^2$ for a 1 W/m^2 incident flux, which agreed well with experimental results

- a zero-frequency transfer function was found for the thermopile detector, which predicted a linear response when the detector was in equilibrium with a steady radiant flux input

- No thermal cross-talk is predicted between adjacent pixels in the linear array detector due to conduction through the detector substrate

- optical cross-talk was compensated for through use of the discrete Green's functions for an input without noise, and a signal with Gaussian noise was recovered with a one percent decrease in the signal-to-noise ratio

- a parametric study of the discrete Green's function, G_{ij}, was performed, and it was determined that G_{ij} decreases as both the specularity ratio and absorptivity increase for the case of $i \neq j$, and G_{ij} decreases as the absorptivity increases but increases as the specularity ratio increases for the case $i = j$.

6.0.2   Recommendations for further research

Suggestions for areas of further research include:

- further studies should be made into the nature and behavior of the discrete Green's functions in radiometric cavities containing detector arrays for various geometries and surface properties

- different geometries and materials should be developed to increase the performance of the thermopile detector, including but not limited to absorber materials

- prototype thermopile detectors should be further tested to provide a more complete characterization of their performance

- diffraction effects should be integrated into the end-to-end model of the cavity radiometer

- the optical cavity model should be used in conjunction with the discrete Green's function to measure the values of absorptivity and specularity ratio.

References

ALGOR, 1993, Standard User's Manual.

Barreto, J., 1998, "Experimental Design for Estimating Electro-Thermophysical Properties of a Thermopile Thermal Radiation Detector," M.S. Thesis, Virginia Polytechnic Institute and State University.

Foote, M. C., Jones, E. W., and Caillat, T., 1998, "Uncooled Thermopile Infrared Detector Linear Arrays with Detectivity Greater than 10^9 $cm\,Hz^{1/2}/W$," *IEEE Transactions on Electron Devices*, Vol. 45, No. 9, pp. 1896–1901.

Gibbons, J. and Chakraborti, S., 1992, *Nonparametric Statistical Inference*, Third Edition, Mercel Dekker Inc., New York, NY.

Gray, J., 1994, "Green and Green's Functions," *The Mathematical Intelligencer*, Vol. 16, No. 1, pp. 45–47.

Green, G., 1828, "An Essay on the Application of Mathematical Analysis to the Theories of Mathematics and Magnetism," Nottingham, England.

Haeffelin, M., 1997, "Introduction to Atmospheric Science," ME 4984, Virginia Polytechnic Institute and State University.

Harris Semiconductors, 1993, "HA-5127 Ulta-Low Noise Precision Operational Amplifier," Harris Corporation.

Huang, B., 1990, "A Precise Measurement of Temperature Difference Using Thermopiles," *Experimental Thermal and Fluid Science*, Vol. 3, No. 3, pp. 265–271.

Kist, E., 1998, Personal communication.

Krieder, K., 1994, "Intermetallic Thermocouples," United States Patent, Patent Number 5,356,485.

Lang, W., Kühl, K., and Sandmaier, H., 1991, "Absorbing Layers for Thermal Infrared Detectors," *TRANSDUCERS '91. 1991 International Conference on Solid-State Sensors and Actuators*, pp. 631–4.

Lenoble, J., 1993, *Atmospheric Radiative Transfer*, A. DEEPACK Publishing, Hampton, Virginia.

Mahan, J. R. and Eskin, L. D., 1984, "The Radiation Distribution Factor - Its Calculation Using Monte Carlo and Example of Its Application," *First UK National Heat Transfer Conference*, pp. 1001–1012, July 4-6, Leeds, Yorkshire, England.

Mahan, J. R. and Langley, L. W., 1996, "The Geo-Synchronous Earth Radiation Budget Instrument: A Thermopile Linear-Array Thermal Radiation Detector," Proposal submitted to NASA, Hampton, VA.

Mahan, J. R., Weckmann, S., Sánchez, M. C., Sorensen, I. J., Coffey, K. L., Kist, E. H., and Nelson, E. L., 1998, "Optical and Electrothermal Design of a Linear-Array Thermopile Detector for Geostationary Earth Radiation Budget Applications," *SPIE Proceedings, International Symposium on Remote Sensing*, Vol. 3498.

Mueller, J., 1997, "Geostationary Earth Radiation Budget (GERB) Instrument Calibration Plans," *Advances in Space Research*, Vol. 19, No. 9, pp. 1307–16.

Özişik, M. N., 1993, *Heat Conduction*, Second Edition, John Wiley & Sons, New York.

Pollock, D. D., 1985, *Thermoelectricity, Theory, Thermometry, Tool*, ASTM Special Technical Publication, American Society for Testing and Materials, Philadelphia, PA.

Sánchez, M. C., 1998, "Optical Analysis of a Linear-Array Thermal Radiation Detector for Geostationary Earth Radiation Budget Applications," M.S. Thesis, Virginia Polytechnic Institute and State University.

Schmidt, W., 1995, "New Manufacturing Technology Improves Thermopile Sensors," Laser Focus World, August.

Sharma, A. and Cogley, A. C., 1982, "Radiative Heat Transfer in a Completely General Plane-Parallel Environment," *International Journal of Heat and Mass Transfer*, Vol. 25, No. 4, pp. 523–534.

Smith, S. M. and Howitt, R. V., 1986, "Survey of Material for an Infrared-Opaque Coating," NASA Technical Memorandum 88204.

Weckmann, S., 1997, "Dynamic Electrothermal Model of a Sputtered Thermopile Thermal Radiation Detector for Earth Radiation Budget Applications," M.S. Thesis, Virginia Polytechnic Institute and State University.

Vita

Ira Joseph Sorensen was born May 26, 1972, in Reedley, California. He attended Selma High School, from which he graduated in 1990. He received a Bachelor of Science in Mechanical Engineering from California Polytechnic State University, San Luis Obispo, where he was a member of Tau Beta Pi and an officer of ASME, in 1996. He relocated to Blacksburg, Virginia, in 1997 to begin his graduate studies at Virginia Polytechnic Institute and State University. Over the course of his graduate studies, he served as a research assistant in the Thermal Radiation Group, as well as a NASA Langley Researcher Summer Scholar (LARSS) and a NASA Graduate Student Researcher Program (GSRP) fellow. He received his Master of Science in Mechanical Engineering in December, 1998. He plans to continue his graduate studies in the Thermal Radiation Group to obtain his Ph.D.